arXiv:1401.0605v3 [astro-ph.GA] 17 Feb 2014

Tracing the Outflow of a z=0.334 FeLoBAL: New Constraints from Low-Ionization Absorbers in FBQS J1151+3822

Adrian B. Lucy and Karen M. Leighly[1]

Homer L. Dodge Department of Physics and Astronomy, The University of Oklahoma, 440 W. Brooks St., Norman, OK 73019

Donald M. Terndrup[1]

Department of Astronomy, The Ohio State University, 4055 McPherson Laboratory, 140 W. 18th Ave., Columbus, OH 43210

Matthias Dietrich[1]

Department of Physics and Astronomy, Ohio University, Clippinger Labs 251B, Athens, OH 45701

and

Sarah C. Gallagher

Department of Physics & Astronomy, The University of Western Ontario, London, ON, N6A 3K7, Canada

Received _____; accepted _____

Accepted for publication in ApJ

ABSTRACT

We show for the first time that FBQS J1151+3822 is an iron low-ionization broad absorption line quasar (FeLoBAL QSO), the second-brightest and second-closest known example of this class. He I* and Fe II together act as an effective analytical tool, allowing us to obtain useful kinematic constraints from photoionization models of the outflow without needing to assume any particular acceleration model. The main outflow's log ionization parameter is -1.5, the log hydrogen density (cm^{-3}) 5.5–8, the log hydrogen column density (cm^{-2}) 21.7–21.9, the absorption radius 7.2–127 pc, and the kinetic luminosity 0.16%–4.5% of the bolometric luminosity. We obtain line-of-sight covering fractions of ~ 0.25 for strong Fe II, ~ 0.5 for He I*, and ~ 0.6 for Mg II. Narrower and shallower absorption lines from weaker Fe II and Mn II with outflow velocity $\sim 3400\,\mathrm{km\,s^{-1}}$ have appeared between 2005 and 2011, suggesting that dense cores may have condensed inside the main outflow. Consideration of the literature might suggest that the FBQS J1151+3822 outflow is a member of a rare and distinct subclass of FeLoBALs with high densities and correspondingly small absorption radii. We find, however, that such outflows are not necessarily a distinct subclass, and that their apparent rarity could be a symptom of selection bias in studies using density-sensitive lines.

Subject headings: quasars: absorption lines — quasars: individual (FBQS J1151+3822)

1. Introduction

A substantial fraction of quasars exhibit broad, blue-shifted absorption lines in their rest-frame UV spectra: manifestations of tempestuous winds, emerging from the central engine at up to thousands of kilometers per second (Weymann et al. 1991). These broad absorption line quasar (BALQSO) outflows can distribute chemically enriched gas through the intergalactic medium (Cavaliere et al. 2002), facilitate accretion by carrying away angular momentum (Emmering et al. 1992; Konigl & Kartje 1994), and inject kinetic energy into the host galaxy, perhaps suppressing star formation (Scannapieco & Oh 2004; Farrah et al. 2012). As such, determining their structure and kinetic power is essential for understanding the physics of supermassive black hole accretion disks and for discriminating between different models of galaxy evolution.

BALQSOs have been divided into three classes based on their spectral properties. High-ionization BALQSOs (HiBALs) have absorption lines from high-ionization species such as C IV. Low-ionization BALQSOs (LoBALs) have the same high-ionization lines as HiBALs, but also have absorption from lower-ionization species such as Mg II (Voit et al. 1993). Finally, FeLoBALs have the same lines as LoBALs, but also have absorption from Fe II (Hazard et al. 1987; Becker et al. 1997). HiBALs are the most common type of BALQSO, comprising perhaps 10–26% of quasars, while FeLoBALs are the least common type, comprising at most $\sim 1\%$ of quasars (Trump et al. 2006; Gibson et al. 2009). As we will argue in the course of our photoionization analyses, the appropriate physical interpretation of BALQSO subclasses relates to the column density of the outflowing gas relative to the size of the H II region; for a given ionization parameter, HiBAL outflows have the smallest column, LoBAL outflows have a larger column (but Mg II LoBALs can

[1]Visiting Astronomer, Kitt Peak National Observatory, which is operated by the Association of Universities for Research in Astronomy (AURA) under cooperative agreement with the National Science Foundation.

still be truncated before the hydrogen ionization front is breached), and FeLoBAL outflows have the largest column (thicker, at least marginally, than the H II zone).

FeLoBALs are of particular interest, in part as a flashpoint in the broader debate over BALQSO unification. There are two limiting models used to explain the rarity of LoBALs relative to HiBALs, and the more dramatic rarity of FeLoBALs: an orientation model wherein the lines of sight through which a high column would be observed subtend a small solid angle (see, e.g., Green et al. 2001; Gallagher et al. 2006; Morabito et al. 2011, for supporting evidence), and an evolutionary model wherein LoBALs and FeLoBALs are a short-lived stage in the lifetime of a young quasar outflow dispersing its shroud of dust and gas (Voit et al. 1993; Becker et al. 2000; Gregg et al. 2006) and suppressing (Farrah et al. 2012) high star formation rates (Farrah et al. 2007; Canalizo & Stockton 2001). This dichotomy of theory motivates detailed investigation into the geometry and kinetic power of FeLoBALs, the rarest class of BALQSO.

In 2008, we observed the nearby ($z = 0.334$), luminous ($M_V = -25.5$) quasar FBQS J1151+3822 using the NASA Infrared Telescope Facility (IRTF), and presented our results in Leighly et al. (2011). We serendipitously discovered a He I*λ10830 (2s$\rightarrow$2p) BAL. The He I*λ3889 (2s$\rightarrow$3p) BAL has been seen in a number of quasars and utilized to great effect (Korista et al. 2008; Arav et al. 2008; Dunn et al. 2010; Borguet et al. 2012), but this was the first time that the 10830Å component had been reported. In that paper, in order to obtain useful (i.e., to within an order of magnitude or so) parameter constraints (on, e.g., ionization parameter, density, column density, radius, and kinetic luminosity) from the limited information afforded by He I* alone, we assumed acceleration by radiative line driving—one of several possible accelerating mechanisms, as discussed in §4.2 of that paper, whereby photons from the central engine resonantly scatter with atoms in the outflow and thereby impart their momentum to the flow. Through a dynamical argument presented in

§4.2 of that paper, this assumption yielded a lower limit on the density, without which our absorption radius and kinetic luminosity constraints spanned many orders of magnitude.

In 2011 May, we observed FBQS J1151+3822 using the KPNO 4-meter telescope equipped with the RC spectrograph, covering 2371-4340Å in the rest frame. Our spectrum, reduced in §2, reveals for the first time that FBQS J1151+3822 is an FeLoBAL, featuring Fe II and Mg II BALs in the previously unobserved wavelengths short of $\sim$ 2845Å. Interested in how these lines could complement the information gleaned from our prior analysis of He I* lines in this object, we performed phenomenological spectral fits in §3, with template analysis based on the He I* lines. *Cloudy* photoionization simulations and partial covering analysis, leading to physical spectral models, are described in §4. In that section, we extrapolate constraints on the geometry and kinetic parameters of the outflow, with Fe II allowing us to drop our assumption of acceleration by radiative line driving; He I* and Fe II together amount to a powerful analytical tool, with He I* pinpointing the ionization parameter, and Fe II (along with other once-ionized iron-peak elements) bracketing the hydrogen column range.

We note that the present paper incorporates a significant amendment to our prior analysis of He I* lines; we now include a model of the host galaxy's contribution to the $\sim$ 1 micron continuum, described in Appendix A, which alters the He I* covering fraction but does not affect any other results from Leighly et al. (2011).

In §5.1, we note that this type of analysis, with enough ions, could potentially obtain the distribution of hydrogen column as a function of covering fraction and build a model of inhomogeneity in the outflow. In §5.2, we compare our target to other FeLoBALs. In §5.3, we argue that the relatively small radius we obtain for the FBQS J1151+3822 outflow is not anomalous or extreme, but only appears to be so due to selection biases in much of the existing literature; we caution against premature assertions regarding the supposed

near-ubiquity of large absorption radii among BAL outflows. A summary is presented in §6.

We used cosmological parameters Ω_Λ=0.73, $\Omega_M = 0.27$, and $H_0 = 71\,\mathrm{km\,s^{-1}\,Mpc^{-1}}$, unless otherwise specified.

2. Observation and Data Reduction

Our spectra were taken during a 2011 May 6–10 observing run at Kitt Peak National Observatory on the Mayall 4-meter telescope. We used the KPC–007 grism (dispersion of 1.39Å per pixel, resolution of 3.5Å, and one of the bluer gratings available, with good sensitivity up to the atmospheric cutoff), the t2ka CCD (gain of 1.4). We observed FBQS J1151+3822 using a blue setting with nominal wavelength coverage between $\sim$ 3200–6000Å. The sensitivity dropped steeply at both ends due to vignetting and, especially, due to the atmospheric cutoff.

Six 15-minute observations were performed, for a total exposure of 90 minutes, as the target passed through the meridian. Atmospheric conditions were not photometric, and the brightness of individual exposures varied by a factor of $\sim$ 1.33. Interestingly, the KPNO spectrum, though it was taken during non-photometric conditions, and the Sloan Digital Sky Survey (SDSS) spectrum (observed 2005 May 11) are almost exactly equal in flux in those regions where they overlap, perhaps suggesting that the target has brightened.

We performed a standard reduction using IRAF. A wide range of flux standard stars were observed; however, the spectra from some of these stars showed peculiar decreases in flux at the ends of the spectra that we believe were caused by the stars not being centered well in the slit. Therefore, only stars observed at the lowest air masses were used for flux calibration. The spectra were combined, weighted by the flux between 4000 – 5500Å. The Galactic reddening in the direction of FBQS J1151+3822 is $E(B-V) = 0.023$

(Schlegel et al. 1998), which we corrected for using the CCM (Cardelli et al. 1989) reddening curve. The NED[2] redshift was listed as 0.3344, and we used that value to correct for cosmological expansion. IRAF spectra do not include errors; FBQS J1151+3822 is a bright object, so we gauged 1-σ errors by assuming Poisson noise in the uncalibrated photon count spectrum. The reduced spectrum and assigned errors are shown in Fig. 1.

In Leighly et al. (2011), we inferred that FBQS J1151+3822 was intrinsically reddened, based on a comparison of the SDSS/MDM spectra and SDSS photometry, with the mean quasar spectral energy distribution (SED) published by Richards et al. (2006). We dereddened by $E(B-V) = 0.1$ using a Small Magellanic Cloud (SMC) reddening law (Pei 1992). For the present work, we addressed the question of reddening more carefully by comparing the FBQS J1151+3822 spectrum with several quasar composite spectra. We found the best match with the updated Francis et al. (1991) quasar composite spectrum created using Large Bright Quasar Sample (LBQS) spectra[3]. We again used an SMC reddening curve, and determined that FBQS J1151+3822 best matches the quasar composite if $E(B-V) = 0.14$. Interestingly, this is the typical value of reddening found for LoBALs by Gibson et al. (2009). In Fig. 1, we show the scaled composite spectrum overlaid with the original and dereddened FBQS J1151+3822 spectra. For comparison, we also show the same for the SDSS spectrum of the $z = 0.7$ broad absorption line quasar FBQS J1044+3656; for that object, we inferred a reddening of $E(B-V) = 0.09$. After dereddening of FBQS J1151+3822, the inferred apparent magnitude is $m_V = 15.4$, and the inferred absolute magnitude is $M_V = -25.8$.

In fact, FBQS J1151+3822 most likely would have been included among the PG quasars were it not for its BAL-related properties (absorption lines in the U band, together

[2]NASA/IPAC Extragalactic Database; http://ned.ipac.caltech.edu/

[3]Available at www.mso.anu.edu.au/pfrancis/composite/widecomp.d.

with intrinsic reddening). The SDSS photometry predicts $U - B = -0.42$, above the nominal PG cutoff of $U - B = -0.44$, and $B = 16.0$, just consistent with the corresponding nominal PG cutoff (Jester et al. 2005). Correcting for emission and absorption lines (as in Appendix A) predicts $U - B = -0.64$ and $B = 15.96$. Correcting for the inferred $E(B - V) = 0.14$ reddening intrinsic to the quasar as well predicts $U - B = -0.69$ and $B = 15.81$. Jester et al. (2005) notes that the effective (median) color cutoff for the PG sample is $U - B = -0.71$. Intrinsically, FBQS J1151+3822 is as bright as a PG quasar.

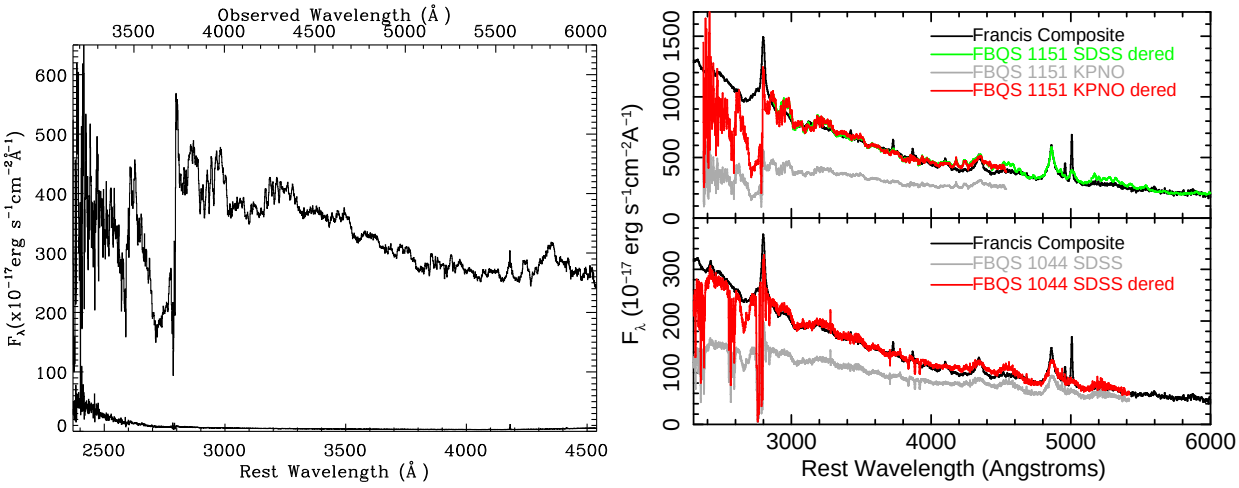

Fig. 1.— The KPNO Mayall 4-meter telescope spectrum of FBQS J1151+3822, as described in §2. The left panel shows the observed spectrum and the assigned uncertainties. The right panel shows the dereddening for FBQS J1151+3822 and for a comparison BALQSO FBQS J1044+3656. We find that the FBQS J1151+3822 continuum is consistent with the Francis composite when dereddened by $E(B - V) = 0.14$ using an SMC reddening curve.

3. Phenomenological Analysis

In Leighly et al. (2011), we described the metastable He I* absorption in FBQS J1151+3822 that was observed both in the infrared at 10830Å and in the optical at 3889Å. However, the optical spectra presented in that paper covered a rest-frame

wavelength range of only 2845–6910Å (SDSS) and 3204–4401Å (MDM). The new KPNO spectrum spans 2371–4340Å in the rest frame, revealing large absorption complexes shortward of Mg IIλ2800, analyzed in §3.1 and §3.3. In addition, new absorption lines have appeared just short of 2960Å, which we describe in §3.4.

3.1. Motivation for Template Analysis

To investigate the origin of absorption, we first needed to determine the level of the unabsorbed continuum (I_0). In Leighly et al. (2011), we noted that the Fe II emission in PG 1543+489 near He I*λ3889 was similar to that of FBQS J1151+3822, and we initially thought to use a spectrum of PG 1543+489 observed at KPNO the same night. The continuum in Fig. 2 is a model of said spectrum with Mg II emission scaled to match that of FBQS J1151+3822.

There are two clearly distinct regions of absorption short of 2800Å. At least some of the absorption between $\sim$ 2650 and 2800Å must be due to Mg II, so the right panel of Fig. 2 plots apparent optical depth for this region as a function of velocity from the oscillator-strength-weighted mean rest wavelength of the Mg IIλ2800 doublet, using $I/I_0(v) = exp(-\tau(v))$. The strongest of the many lines possible in the other absorption region (predominately transitions from the ground term of Fe II) would absorb from ground state Fe II at 2600Å, so we likewise plot the apparent optical depth between $\sim$ 2540 and 2600Å as a function of velocity from 2600Å. For comparison, we overlay the apparent optical depth of the He I*λ10830 line reported in Leighly et al. (2011).

This plot reveals several salient properties of the absorption shape between $\sim$ 2650Å and 2800Å. Most obviously, it is significantly broader than the He I* absorption trough. He I* is absorption from a neutral atom, but because metastable helium arises from

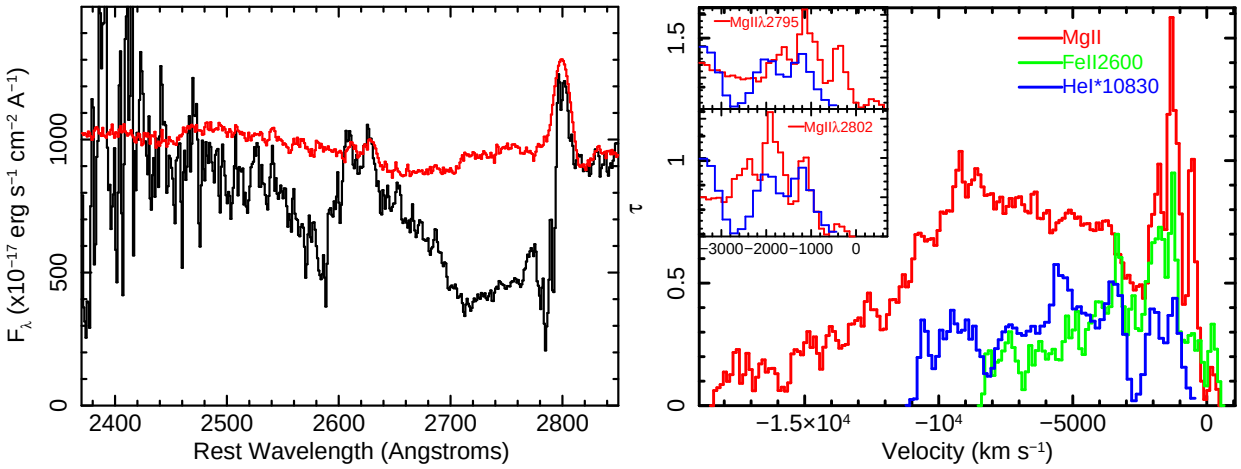

Fig. 2.— Preliminary continuum and apparent optical depths for the absorption lines. The left panel shows the dereddened FBQS J1151+3822 spectrum overlaid with the continuum model developed from our PG 1543+489 spectrum. The right panel shows the inferred apparent optical depths for the feature spanning $\sim$ 2650 to $\sim$ 2800Å (in red), if the whole feature is attributed to the Mg II doublet, and the feature between $\sim$ 2540 and $\sim$ 2600Å (green) if attributed to the strong Fe II ground-state transition at 2600Å, compared with the He I*λ10830 apparent optical depth profile (blue) derived in Leighly et al. (2011). Significant structural similarities between these profiles are observed, while the breadth of the Mg II suggests contamination by excited-state Fe II on its blue wing. The insets show the low-velocity features from the rest wavelengths of the individual lines forming the Mg II doublet.

recombination onto He^+, this absorption occurs in roughly the same gas that would produce the generally-prominent C IV BAL. That is, He I* acts as a high-ionization line, while Mg II is a low-ionization line. High-ionization lines are generally broader, and extend to higher velocities, than low-ionization lines (Voit et al. 1993); if this feature originated in Mg II only, its breadth relative to He I* would be very anomalous. Excited-state Fe II, then, is the most plausible origin for the short-wavelength end of this feature; we show in §4.4 that Cr II and Ti II, the only other conceivable absorbers on the blue wing of Mg II, can at most produce a small fraction of the observed opacity.

There are several narrow absorption features near 2800 Å, including those at ~ -1870,

-1260, -580, and $+210\,\mathrm{km\,s^{-1}}$ from the mean rest wavelength of the Mg II doublet. The velocity separation of the Mg II doublet is $769\,\mathrm{km\,s^{-1}}$, and the two lowest-velocity features, which are relatively narrow, have this separation. They thus appear to be low-velocity associated absorption with $v \sim 390\,\mathrm{km\,s^{-1}}$, unrelated to the BAL outflow, and we interpolate over them for fits throughout this paper. The features at ~ -1870 and $\sim -1260\,\mathrm{km\,s^{-1}}$ are separated by only $\sim 610\,\mathrm{km\,s^{-1}}$, and thus cannot be attributed to the doublet structure of Mg II. These features are echoed in the Fe II opacity shortward of 2600Å. The He I* profile, similarly, has two low-velocity components; however, as shown in Fig. 2, these do not line up perfectly with the KPNO spectrum features.

Despite the differences, we suggest that the profile of He I* is more similar to those of Mg II and Fe II than it is different; in particular, there is a suggestive low-opacity region in all said profiles at $\sim 2700\mathrm{km\,s^{-1}}$. Due to significant line blending within Fe II multiplets in the bandpass of the KPNO spectrum, and the blending of Mg II with excited-state Fe II as noted above, we could not hope to deconvolve the line contributions and extract ionic columns without using some non-blended absorption line as a template. Blending also precluded modeling individual velocity components of the outflow as independent gases. We therefore used the He I* profiles as templates in the following analyses.

3.2. The Continuum

While the Fe II emission in PG 1543+489 resembles that of FBQS J1151+3822, our KPNO spectrum shows dramatic differences in multiplet strength at shorter wavelengths. UV Fe II emission complexes are known to display a variety of shapes (e.g., Leighly & Moore 2006; Leighly et al. 2007). Therefore, we created customized continua for FBQS J1151+3822. This object has especially strong and blocky Fe II features between 2900 and 3000Å. We used spectral fit results from an unpublished catalog of 5307 SDSS

spectra (chosen because it had enough spectra with emission structures matching our object) in the z=1.2–1.8 range, selecting quasars with relatively narrow Mg II emission lines (to match that of FBQS J1151+3822) and no broad absorption lines (to reveal the continuum). We identified a set of objects that had similarly large, blocky $\sim$ 2950Å features.

After experimenting with several composite continua, we settled on one constructed from 12 objects with large iron equivalent widths (between 50 and 180Å) and with narrow Mg II ($< 2400\,\mathrm{km\,s^{-1}}$). This is the continuum model appearing in every panel of Fig. 3. To estimate the systematic uncertainties associated with our choice of continuum, we fit our spectrum with this continuum, the PG 1543+489 continuum, and one other constructed using quasars from the above catalog with the strongest Fe II. As reported in §3.3.3, continuum-related systematic uncertainty in fit results is relatively small.

3.3. Modeling the Apparent Absorption Short of 2852 Å

Here, we describe our extraction of the apparent column densities of ions absorbing between 2481 (where the statistical error in our spectrum stabilizes into a smooth descent) and 2852Å (the rest wavelength of a possible Mg I BAL). To achieve this extraction, we made the assumptions—the utility of which will become evident via §4 photoionization models—that all opacity fully and homogeneously covers the continuum, and is produced by the strongest BALQSO absorbers in this region: Fe II lines from less than 2.5 eV above the ground state, the Mg IIλ2800 doublet, and perhaps the Mg Iλ2852 line.

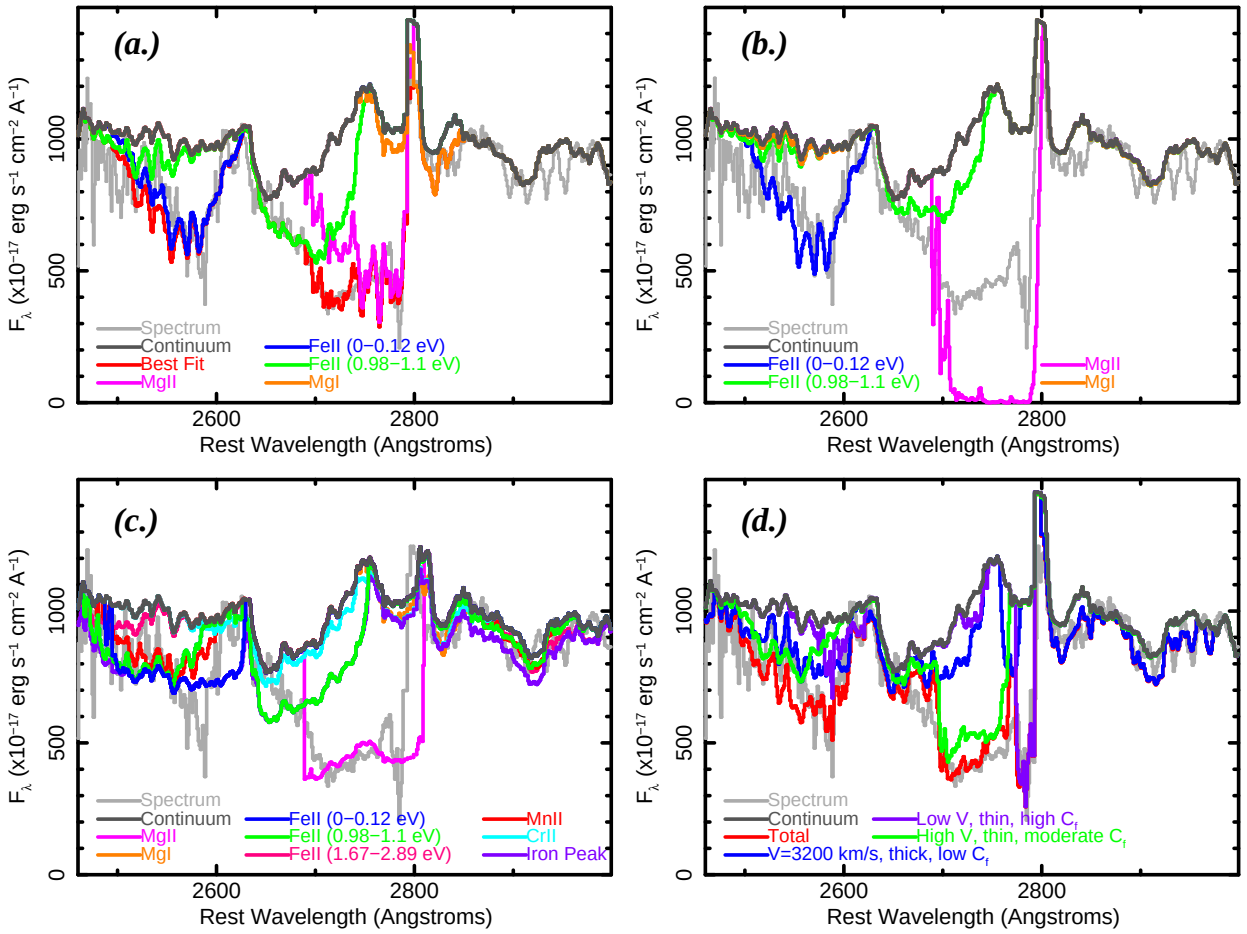

Fig. 3.— (a.) The phenomenological model fit, discussed in §3. High-excitation Fe II is necessary to fit the spectrum just short of Mg II, a region which anchors the high-excitation Fe II fit. (b.) The model spectrum from the figure-of-merit best fit obtained through comparison of the columns obtained through the phenomenological fit and *Cloudy* modeling, as described in §4.2. This model does not match observations because it does not take partial covering and saturation into account. (c.) The model spectrum based on the upper limit analysis described in §4.4, for a covering fraction of 0.58 applied to Mg II and Mg I, and a covering fraction of 0.25 applied to Fe II and other iron-peak ions (Mn II, Cr II). (d.) An ad hoc inhomogeneous model, described in §4.5, that attempts to explain the $\sim$ 2960Å lines without producing excess absorption elsewhere.

3.3.1. Fe II Transitions Considered

Between 2481 and 2852Å, Fe^+ BAL absorption is dominated by four multiplets absorbing from within 2.5 eV of the ground state; these lines are summarized in Table 1 and superimposed on the spectrum in Fig. 4, using NIST[4] atomic data. The upshot of this information, when considered in light of the two distinct absorption regions previously discussed in §3.1, is that Fe II absorption can be split into two sets, with distinct and narrow energy ranges, that are useful for template analysis fits. Absorption from the a ^{6}D term (0–0.12 eV above ground) dominates the absorption complex short of $\sim$ 2600Å. Absorption from a ^{4}D (0.98–1.1 eV) is solely responsible for the blue wing of the Mg II complex, and also contributes to the complex short of $\sim$ 2600Å. For the convenience of readers unfamiliar with the atomic structure of Fe^+, we will henceforth call the a ^{6}D set of lines "Fe II Low," and the more excited a ^{4}D set "Fe II High."

[4]National Institute of Standards and Technology Atomic Spectra Database; http://www.nist.gov/pml/data/asd.cfm

Table 1. Fe II Line Sets

Name	Lower-level Excitation (eV)	Lower-level Term	Lines	Multiplets	Rest λ (Å)
Fe II High	0.98–1.1	a ^{4}D	19	2	2692–2773
			8	1	2562–2612
Fe II Low	0–0.12	a ^{6}D	13	1	2585–2631

This information is comprehensive only for this bandpass, and is not comprehensive for extremely saturated BALs where Fe II absorbs from above 2.5 eV (as in §4.4). We also omit multiplets with line oscillator strengths less than $\sim$ 0.001.

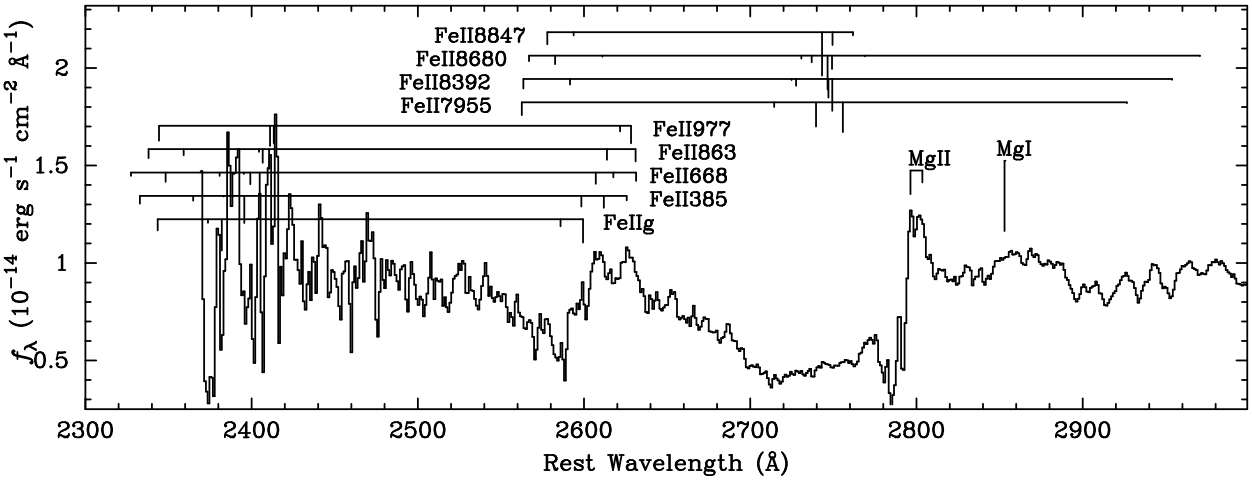

Fig. 4.— The transitions considered in §3.3, along with term-related shorter-wavelength lines that fall outside our band of good data. Fe II lines are grouped by common lower level energy (labeled in cm^{-1}) rather than by multiplet. Only lines with $f_{ik} > 0.005$ are shown. The length of the downward tick mark is proportional to the oscillator strength of the transition with, for visibility's sake, the scaling of Fe II being 2.5 times that of Mg II and Mg I. The iron lines group nicely by wavelength and excitation, with the bottom five energy levels (Fe II Low) dominating short of $\sim$ 2600Å, and the top four energy levels (Fe II High) dominating on the blue wing of Mg II. The observed spectrum towards $\sim$ 2500 Å and shortward is dominated by statistical noise due to the atmospheric cutoff, so any structure there is not real.

3.3.2. Template Analysis

To facilitate a fit of the apparent optical depth that could produce useful results in spite of line blending, we first constructed amalgamated optical depth profiles for Mg II, Fe II Low, and Fe II High. We used the unblended He I* lines as templates to shape these profiles. Korista et al. (1992) and Arav et al. (1999), among others, have previously used templates to de-blend BALs.

Within, for example, the doublet Mg II line set, we weighted each component transition's contribution to the total optical depth of the set as

$$\tau_{j,proto}(v) = R_i \frac{\lambda_j f_j}{\lambda_{He} f_{He}} \tau_{He}(v). \quad (1)$$

Here, $\tau_{j,proto}$ denotes a weighted optical depth for a transition j with lower energy level i, as a function of velocity v. $\tau_{He}(v)$ is the He I* profile used as a template. For the simple case of Mg II, where both doublet lines arise from the same lower level i, $R_i = 1$ and the relative strength of each line j depends only on the product of the wavelength and oscillator strength of the line, $\lambda_j f_j$ (Savage & Sembach 1991). For computational convenience, we also divided by the He I* template line's $\lambda_{He} f_{He}$.

Then we resampled each $\tau_{j,proto}(v)$ onto a wavelength scale, with velocity giving blueshift from the rest wavelength of each line j. The net effect was a Mg II optical depth profile shape that, as seen (along with Fe II Low and Fe II High) in the top row of Fig. 5, took into account the relative strengths of the component doublet lines, and could be fit to the spectrum with a parameter linearly scaling the optical depth $\tau(\lambda)$.

For Fe II Low and Fe II High, wherein each of the many lines do not all arise from the same lower level, we defined the weighting factor R_i: the ratio of the level i population to the population of the lowest-energy level in the set. We used level population ratios R_i from *Cloudy* modeling (anticipating our more careful *Cloudy* constraints in §4). The lines within each set arise from a very small range of energy levels, and species in a photoionized gas are in approximate LTE when the density is above their critical densities, so these ratios were approximately equal to the ratios of the levels' degeneracies.

To estimate systematic uncertainties associated with the template shape, we tried each of the five different $\tau_{He}(v)$ derived from FBQS J1151+3822 in Leighly et al. (2011), including the saturated (and hence covering fraction dominated) 10830Å profile and four different estimates of the shallow 3889Å profile described in that paper. As reported in the following section, this template-related uncertainty is relatively small. The spectral models shown in Fig. 3 use the MDM-28 He I*λ3889 profile described in Leighly et al. (2011), because it yields slightly better fits than the others.

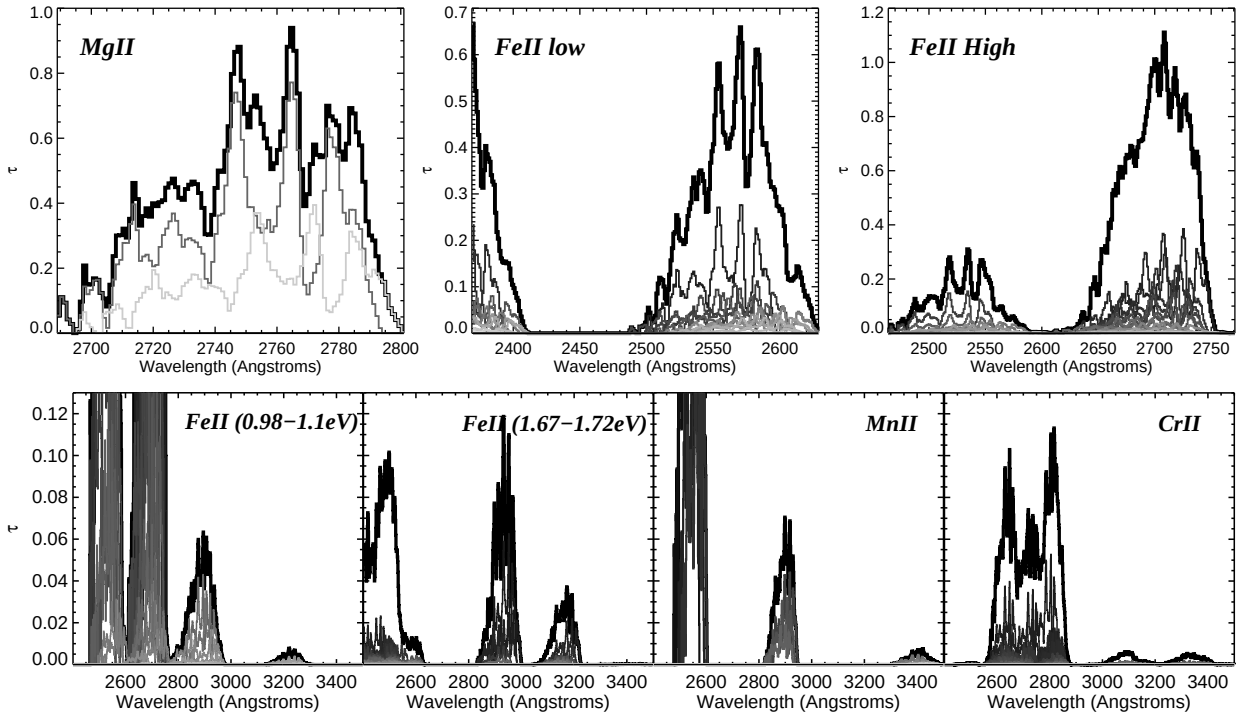

Fig. 5.— Development of the composite absorption profiles; the top panels pertain to profiles used for fitting in §3.3, while the bottom panels pertain to the $\log(N_H) - \log(U) = 23.4$ upper limit in §4.4. In each panel, the composite profile is shown in the thick black line, while the components making up that profile are shown in shades of gray.

3.3.3. Spectral Fitting Results

We used the IRAF contributed-program `Specfit` (Kriss 1994) to fit the spectrum. This program allows the user to input continua, Gaussian emission lines (in our case, two Mg II lines), and profiles of optical depth as a function of wavelength (in our case, Fe II Low, Fe II High, Mg II, and for our two strong-iron-emission composite continua, Mg I). It outputs the χ^2 best fit linear scaling normalizations for the inputs, along with statistical uncertainties. We performed 15 fits, with each of the three continua and five templates previously mentioned. All normalizations were allowed to vary, except for that of the PG 1543+489 model continuum. Uncertainties in all varying normalizations were

propagated into each other. All features were fixed in wavelength.

A representative spectral fit, using the previously mentioned preferred continuum (§3.2) and template (§3.3.2), is shown in the top-left panel of Fig. 3. The usefulness of splitting Fe II into the Low and High groups is clear to see in this fit, where Fe II High is anchored by the spectrum just short of Mg II.

We used the output normalizations to extract the net apparent column densities of the relevant sets of species: Fe^+ Low (0-0.12 eV), Fe^+ High (0.98-1.1 eV), ground-state Mg^+, and ground-state Mg^0. The gist of this calculation is given in Equation 9 of Savage & Sembach (1991); i.e., for a given energy level i, the apparent column density of level i is

$$N_i = \frac{m_e c}{\pi e^2} \frac{1}{\lambda_j f_j} \int \tau_j(v) dv, \tag{2}$$

where m_e is the electron mass, e is the electron charge, c is the speed of light, and τ_j is the fitted apparent optical depth of a single line j from level i. `Specfit` modeling output the optical depth normalization S for each absorption profile (Mg II, Fe II Low, Fe II High, Mg I). We used Equation 1 to define the fitted optical depth for each of these as

$$\tau_j(v) = S\tau_{j,proto}(v) = SR_i \frac{\lambda_j f_j}{\lambda_{He} f_{He}} \tau_{He}(v). \tag{3}$$

Combining Equation 2 and Equation 3, and summing over energy levels, the total column density for the level set (the sum of the column densities for all components of, e.g., Fe II Low), is

$$N = \sum_i N_i = S\Big(\sum_i R_i\Big) \frac{m_e c}{\pi e^2} \frac{1}{\lambda_{He} f_{He}} \int \tau_{He}(v) dv. \tag{4}$$

These apparent column densities, along estimated errors, are given in the first row of Table 2. The reported column densities are the median results from our 15 fits, and the reported errors delineate the full range from the maximum column plus statistical error to the minimum column minus statistical error (altered in a conservative way to be symmetric

Table 2. Measured and Modeled Low-Ionization Column Densities

Ion	Energy	Log_{10} Column		
		Apparent[a] (§3.3)	Lower Limit (§4.2)	Upper Limit (§4.4)
Fe II Low	(0–0.12 eV)	15.29 ± 0.1	15.38	17.64
Fe II High	(0.98-1.1 eV)	14.89 ± 0.1	14.62	16.65
Fe II	(1.67–2.89 eV)	–	–	15.98
Mg II	(0 eV)[c]	15.03 ± 0.1	15.89	17.00
Mg I	(0 eV)	13.8 ± 0.15[b]	13.65	13.65
Mn II	(0 eV)	–	–	14.85
Mn II	(1.17 eV)	–	–	13.86
Cr II	(all)	–	–	16.04

Blanks (–) denote negligible column density, i.e., no effect on the spectrum.

[a]Errors are conservatively altered to be symmetric in log.

[b]Mg I was not required using the continuum with weakest iron emission, so its detection is tentative. The non-detection is ignored in the stated uncertainty.

[c]Virtually all Mg^+ is in the ground state, because its first excited state is ~ 4 eV.

in the log, for convenience in *Cloudy* modeling). Systematic uncertainty dominates over statistical uncertainty in these errors, but nevertheless is very small. For He I* in the ensuing physical analysis, we used the average column density derived in Leighly et al. (2011). However, the errors in the He I* column density obtained in that paper include the uncertainty in the covering fraction as well as the uncertainty in the optical depth; in order for the measurement of the metastable helium column to have equal weight in *Cloudy* model fits, we made the error on He I* commensurate with the other ions at $\log N_{HeI*} = 14.9 \pm 0.1$.

The reduced-χ^2 were much larger than one for all fits, a consequence of including only statistical errors in the modeling when, in fact, systematic errors dominate. However, the fact that the gross features of the spectrum are fit fairly well, and the fact that there is good agreement among the results from various fits, suggest that the measured column densities are of sufficient quality to use as stepping stones to physical constraints in §4.

3.4. Variable Absorption Lines Short of 2960 Å

The SDSS spectrum, taken on 2005 March 3, samples a wavelength range extending down to $\sim$ 2850Å in the rest frame. We show the near UV portion of the new (2011 May) KPNO spectrum overlaid on the SDSS spectrum in Fig. 6. There is a good correspondence overall, but the new spectrum has additional absorption lines just short of 2960Å, and possibly also near 3200Å. We used spectral fitting to measure the centroid positions of the four features near 2960Å: 2896, 2916, 2933, and 2952Å.

These lines were not trivial to identify without additional information. Fortunately, FBQS J1214+2803 (analyzed by de Kool et al. 2002b) has very similar features, slightly shifted in wavelength, and we overlay the SDSS spectrum of that object in Fig. 6. Following the line identifications given by de Kool et al. (2002b), we found that the features

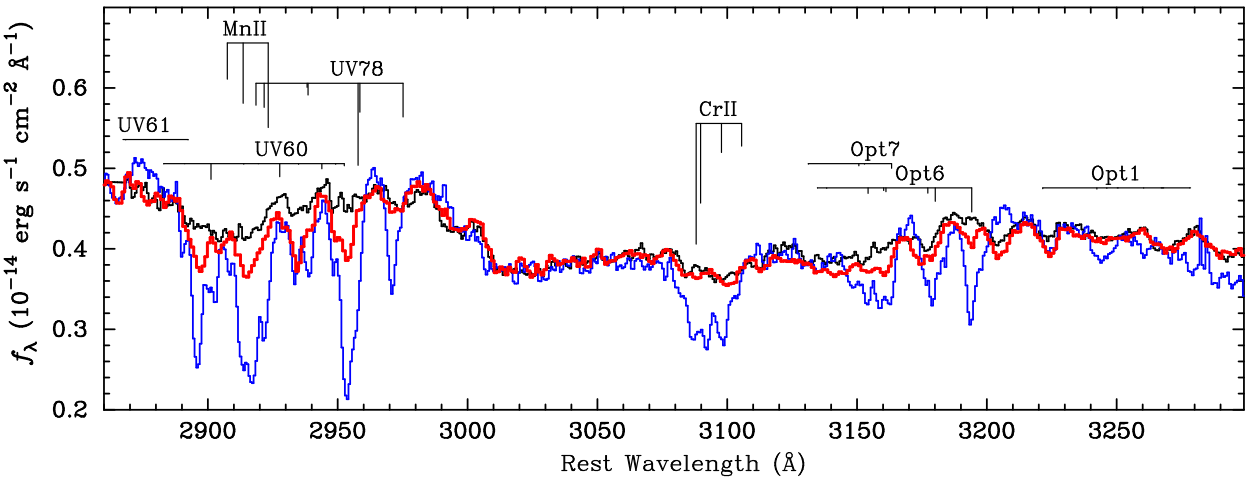

Fig. 6.— New (i.e., variable) narrow absorption lines just short of 2960Å. The 2011 KPNO spectrum of FBQS J1151+3822 (red), the 2005 SDSS spectrum of FBQS J1151+3822 (black), and the SDSS spectrum of FBQS J1214+2803 (blue), which has very similar (albeit stronger) features. Lines from Fe II (labeled with their multiplet designations from Moore (1952)), Mn II and Cr II, shifted by $-3,300\,\mathrm{km\,s^{-1}}$ are marked, where the tick length is proportional to the oscillator strength for each ion. The higher excitation of some of the new multiplets requires a high density, suggesting the condensation of dense cores in the outflow as discussed in §4.5.

near 2960Å are a combination of excited Fe II from transitions with lower levels near 1 and 1.7 eV, and excited state Mn II with lower levels near 1.2 eV, with a blueshift of around $3400\,\mathrm{km\,s^{-1}}$.

As discussed in more detail in §4.4, these new lines have very low opacity, a consequence of small oscillator strength, sparsely populated excited states, and/or low abundance (depending on the line in question). Variability apparently limited to low-opacity transitions seems to be unprecedented in the literature. However, we have only one epoch shortward of $\sim$ 2850Å. It may be that high-opacity lines like Mg II and Fe II shortward of 2850Å also vary.

At first glance, and given the velocity width of the He I* lines (e.g., Fig. 2), it is not obvious why relatively narrow lines would appear at the observed velocity offset.

However, the He I* profile can plausibly be broken into two parts, a low-velocity component between $\sim -3,000$ and $-500\,\mathrm{km\,s^{-1}}$, and a high-velocity component between $\sim -11,000$ and $\sim -3,000\,\mathrm{km\,s^{-1}}$. So these narrow features are located at the low-velocity end of the higher-velocity feature. That type of structure—thicker, lower-ionization gas lying at lowest velocities for a given component—appears to be common in BALQSOs (Voit et al. 1993). Furthermore, examination of the dN_{HeI*} as a function of velocity for the partial covering model of Leighly et al. (2011, Fig. 6) shows a suggestive maximum near $-3,300\,\mathrm{km\,s^{-1}}$ that may support higher column density at this velocity.

4. Physical Analysis

In Leighly et al. (2011), we performed *Cloudy* (Ferland et al. 1998, 2013) photoionization simulations to constrain the physical conditions in the gas responsible for the He I* BAL in FBQS J1151+3822, including hydrogen density n (atoms per cm^3), ionization parameter U, and hydrogen column density N_H (per cm^2) — tending to use $\log N_H - \log U$ in place of this last parameter, so that the hydrogen ionization front lies at a constant value. We found that the ionization parameter had to be higher than $\log U \sim -1.4$ to produce sufficient He I*. Higher-resolution *Cloudy* runs have since reduced that minimum to ~ -1.5. The number density was constrained to be less than $n \sim 10^8\,\mathrm{cm^{-3}}$ by the absence of Balmer absorption lines in our spectra. We could not further constrain the gas parameters directly, although we made a dynamical argument for a minimum density of $\log n \sim 7$ under the assumption that the outflow was accelerated by radiative line driving.

In this section, using the same *Cloudy* setup, we describe further constraints on the gas properties imposed by the low-ionization absorbers in our new KPNO spectrum; these allowed us to lift the assumption of acceleration by radiative line driving and still obtain useful constraints.

We did, however, assume step-function/homogeneous covering, except where otherwise noted, so that the ratio of the observed spectrum to the continuum in a single absorption line is given by

$$\frac{I}{I_0} = \exp(-\tau_{app}) = 1 - C_f + C_f \exp(-\tau_{true}) \quad (5)$$

(Hamann et al. 1997; Arav et al. 2005), where τ_{app} is the apparent optical depth considered in §3, C_f is the covering fraction of the absorber, and τ_{true} is the true optical depth. In this model, the apparent columns measured in §3 are a lower limit for the average column density (the product of true column and covering fraction). As is standard practice (e.g., Sabra & Hamann 2005), we took ionic columns in our photoionization models to refer to this average column, as an implicit compromise between innumerable possible spatial geometries. We explore inhomogeneity in §4.5.

We also assumed *Cloudy*'s default solar abundances, as given in Hazy, the *Cloudy* manual.

4.1. The Utility of the He I*/Fe II Combination

Fig. 7 shows contours of average ion columns[5] with superimposed measurements for these absorbers, as a function of ionization parameter and $\log N_H - \log U$ for a constant density of $\log n = 7$. The measured He I* average column becomes approximately vertical at $\log U \sim -1.5$; here, the He I* column density is ionization bounded near the hydrogen ionization front. That is, for a typical AGN continuum, no He^+ ions exist beyond the hydrogen ionization front, and since He I* is created by recombination onto He^+ (the ratio of metastable He^0 to He^+ is nearly constant), no He I* can exist there either. For normal quasar SEDs, He^+ dominates the ionization balance in the outer portion of the H II region

[5]A similar plot appears in the proceedings paper Leighly et al. (2012).

(e.g., Fig. 1 in Hamann et al. 2002). Like hydrogen, for a semi-infinite slab, the amount of He^+ depends nearly linearly on the ionization parameter. The more intense the photon field, the larger the H II region, the more ionized helium ions are present, and the more metastable helium ions are present. So the measured He I* column density sets a lower limit on the ionization parameter.

Hence, at the minimum $\log U \sim -1.5$, He I* attains the measured average column at the hydrogen ionization front, and increasing the column density beyond the front cannot increase the He I*. This is not true for ionization parameters > -1.5; there, the gas must be matter bounded (truncated somewhere before the hydrogen ionization front) in order to not exceed the measured He I* average column density.

The Mg II and Fe II column density contours are approximately parallel to the hydrogen ionization front; to produce these low-ionization lines with a high ionization parameter, there simply needs to be a commensurately high hydrogen column. Fe II is very rare in the gas for lower values of $\log N_H$ at a given $\log U$, becoming significant only by the vicinity of the hydrogen ionization front.

These properties imply that the combination of He I* plus Fe II together provide unparalleled constraints on both column density and ionization parameter. Some of the diagnostic powers of this combination have previously been noted by, e.g., Korista et al. (2008). Here, however, we emphasize that the ions occur in disjoint regions of the gas; He I* requires He^+ to be present, and that is only found in the H II region, while Fe II requires penetration of the hydrogen ionization front; the presence of Fe II implies that He I* is ionization bounded. So where both He I* and Fe II are present, as they are in our object, the former's column yields the specific ionization parameter, and the latter's column constrains the hydrogen column.

Given these tools, even a cursory glance at the He I* and Fe II panels of Fig. 7 will

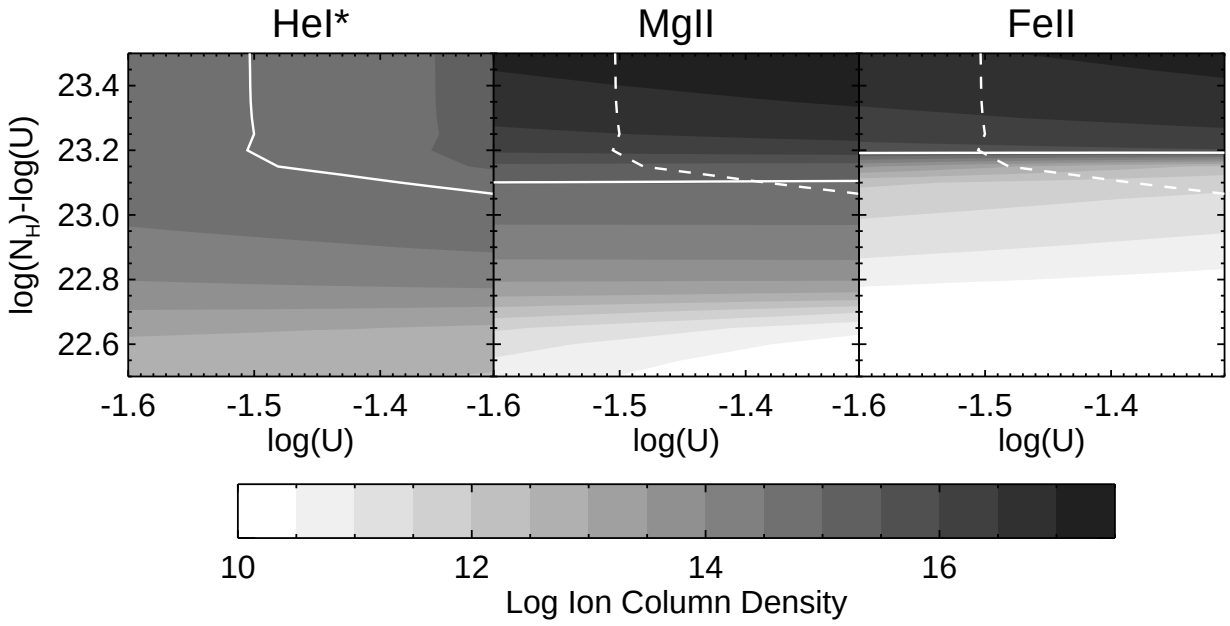

Fig. 7.— Investigation of *Cloudy* parameter space, discussed in §4.1. Each panel shows shaded contours of ion column density. The white solid contours show our measured average (He I*) and apparent (Mg II, Fe II) column densities of the various ions, where Fe II is the sum of Fe II Low and Fe II High. The dashed white contours replicate the He I* measured average column contour for comparison. The intersection of the He I* and Fe II white contours show that $\log U \sim -1.5$ and that $\log N_H - \log U$ is at least ~ -23.2. The Mg II white contour is below this intersection, indicating Mg II saturation.

correctly suggest that $\log U \sim -1.5$ and that $\log N_H - \log U$ is at least ~ -23.2. Then, in light of these requirements, the Mg II panel implies that the measured Mg II apparent column is definitely less than its average column by a factor large enough to imply that it is saturated; in contrast, the Fe II apparent column is not obviously inconsistent with the model.

4.2. Figure-of-Merit Fit from the Measured Columns

Following up on these suppositions, our next step was to find the gas parameters that best fit the measured columns, using a figure-of-merit analysis. For our figure of merit,

we used the absolute value of the difference between the measured ion column densities and the *Cloudy* model column densities, divided by the measurement uncertainty in the column density. We had used a similar figure of merit previously (Casebeer et al. 2006; Leighly 2004), and found that it handles outliers better than χ^2, although the statistical significance of the value is not as clear. We considered the average column density of He I*, the apparent column densities of Fe II Low, Fe II High, and Mg I, and the upper limit on Balmer absorption obtained in Leighly et al. (2011). Since Mg II is unambiguously saturated, we excluded its apparent column from the fit.

The results are shown in Fig. 8. The left side of Fig. 8 shows contours of the figure of merit. The + sign marks the position of merit minimum, located at $\log U = -1.5$, $\log n = 7.2$, and $\log N_H - \log U = 23.18$ (corresponding to $\log N_H = 21.68$); the middle row of Table 2 lists the predicted ion columns at this best fit. The white areas are regions in which the Balmer absorption upper limit would be violated. As expected, column densities below the best fit are strongly excluded due to the Fe II behavior discussed in the preceding section.

The right side of Fig. 8 shows contours of ionic column density as a function of the gas properties. The solid contours show where the observed ionic column density equals the model ionic column density, while the shaded regions of the same color show the measurement uncertainty ranges.

The middle-right panel shows that the data impose interesting constraints on the number density. As noted by, e.g., Korista et al. (2008), excited state Fe II lines have critical densities around $\log n \sim 4.5$, while ground-state iron does not have this restriction. This means that very little Fe II High is present in the gas for log densities lower than ~ 5. But for log densities higher than ~ 6, the Fe II Low and Fe II High contours begin to approach one another, then run nearly parallel to each other through high densities, up

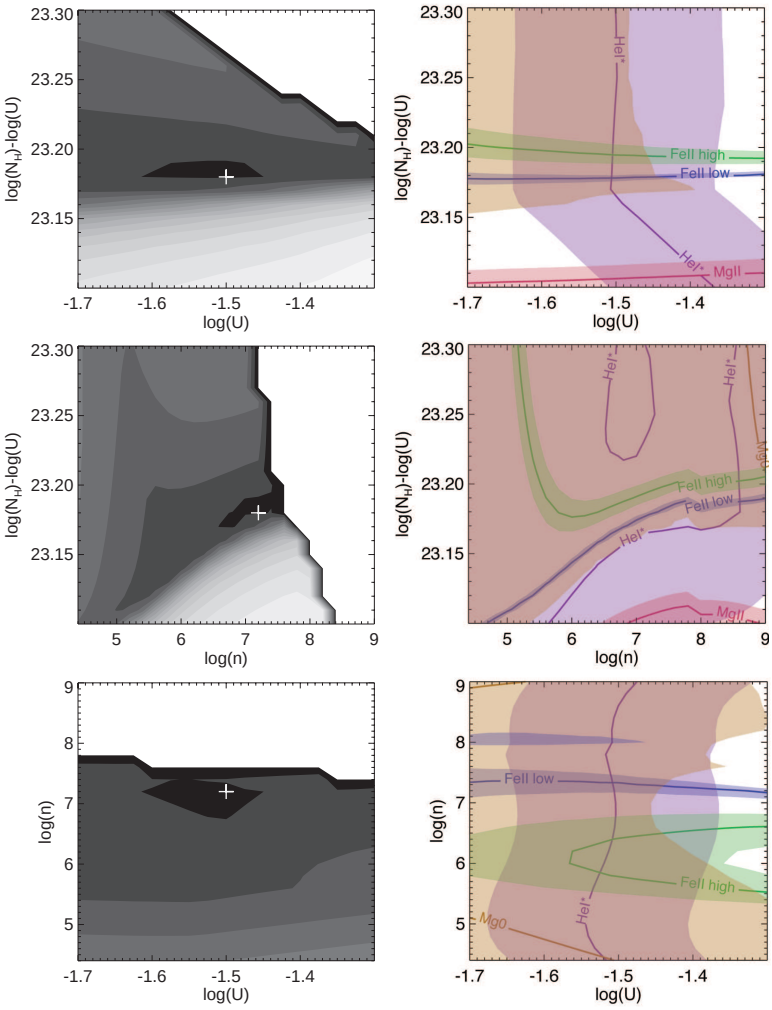

Fig. 8.— The results of the figure-of-merit analysis, showing contours through cross sections of parameter space centered around figure-of-merit minimum marked by the plus sign and located at $\log U = -1.5$, $\log n = 7.2$, and $\log N_H - \log U = 23.18$, corresponding to $\log N_H = 21.68$. The left side shows contours of the figure of merit. The white regions show where the predicted Balmer absorption is larger than the upper limit implied by non-detection of Hα absorption (Leighly et al. 2011), and are therefore ruled out. The strong gradient of the contours bordering that region are an artifact of the plotting program. The right side shows the contours of the column densities of the measured ions. The solid line shows the measured value, and the shaded areas show the uncertainty range. The contours are colored as follows: He I* is purple, Fe II Low is blue, Fe II High is green, Mg II is red, and Mg I is taupe. As discussed in §4.2, the Fe II High and Low contours on the right side suggest useful constraints on $\log n$, while the non-intersection of these two contours hints that Fe II may be saturated.

to and beyond the limit imposed by the lack of Balmer absorption. The top-right panel, likewise, illustrates the robust constraints on ionization parameter imposed by He I*.

The right panels also constitute our first intimation that Fe II is saturated; if the Fe II apparent columns were approximately equal to the average columns, Fe II High and Fe II Low contours or their error bars would overlap. They do not.

We created $C_f = 1$ spectral models using the ionic columns from *Cloudy* at the figure-of-merit minimum, together with the templates and continua discussed in §3.3. That is, inverting the procedure described in §3.3.3, we took the *Cloudy* ion columns and calculated the corresponding scaling factors for the optical depth profiles. These models, exemplified in the upper-right panel of Fig. 3, demonstrated that Mg II is completely saturated, and reaffirmed that the *Cloudy* figure-of-merit best fit predicts insufficient Fe II High.

4.3. Fe II Saturation Near the H Ionization Front

As discussed above, our best-fitting *Cloudy* model predicts too little Fe II High relative to Fe II Low. To investigate this further, we searched parameter space for physical conditions that would produce columns of Fe II closer to the measured apparent columns. The measured columns from the phenomenological fit (§3.3.3) predict a ratio of 2.5 for the columns of Fe II Low / Fe II High. However, the figure-of-merit best fit in *Cloudy* parameter space (see §4.2) yielded a ratio of 5.6. Broadening the search to minimize the figure-of-merit over *only* Fe II species (i.e., $|FeIILow(obs) - FeIILow(Cloudy)| + |FeIIHigh(obs) - FeIIHigh(Cloudy)|$), we found a ratio of 5.0, still a factor of two higher than the ratio measured and barely better than 5.6. Thus, anywhere in parameter space that would produce the right amount of Fe II Low

column density, too little Fe II High is predicted.

To explore this discrepancy further, we show in Fig. 9 the ratios of model-data to the continuum for He I*λ10830, Mg II, Fe II Low, and Fe II High. Best fit results from spectral fitting, and model results from *Cloudy*, are shown. Despite their different columns and line strengths, the He I*λ10830 and Mg II fits are about as deep as one another, a consequence of the lines being saturated and having roughly similar (though not identical—see §4.4 for Mg II and Appendix A for He I*) covering fractions. Likewise, the two Fe II complexes also reach approximately the same depth as each other, albeit a much lower depth than the Mg II and He I* lines. This suggests that their apparent optical depths are influenced much more by covering fraction than by the optical depth of the gas, and that Fe II Low, and likely Fe II High as well, are saturated.

This result does not appear to be an artifact of the modeling. Differences caused by using other continua are not significant, and nor are our conclusions a consequence of blending with Mg II, since the high-velocity side of Fe II High is unblended (see Fig. 3, upper-right panel).

Indirect support for Fe II Low and Fe II High saturation comes from the right panel of Fig. 10, which shows predicted I/I_0 for various absorption complexes as a function of $\log N_H - \log U$, for our best fit values of $\log U = -1.5$ and $\log n = 7.2$. To construct this figure, we assume a rectangular absorption profile with a velocity width of $5000\,\mathrm{km\,s^{-1}}$; this is loosely equivalent to the profiles we observe, with velocity widths of $\sim 11,000\,\mathrm{km\,s^{-1}}$ and covering fractions of $\sim$50%. I/I_0 features comprised of multiple lines were treated as a single line characterized by the sum of the τ values for each line; this is an approximation, since opacity from a group of lines will be spread over a larger wavelength than a single line, but plot is meant to be qualitative.

In this plot, I/I_0 values for the Fe II complexes drop, and then level off to saturation,

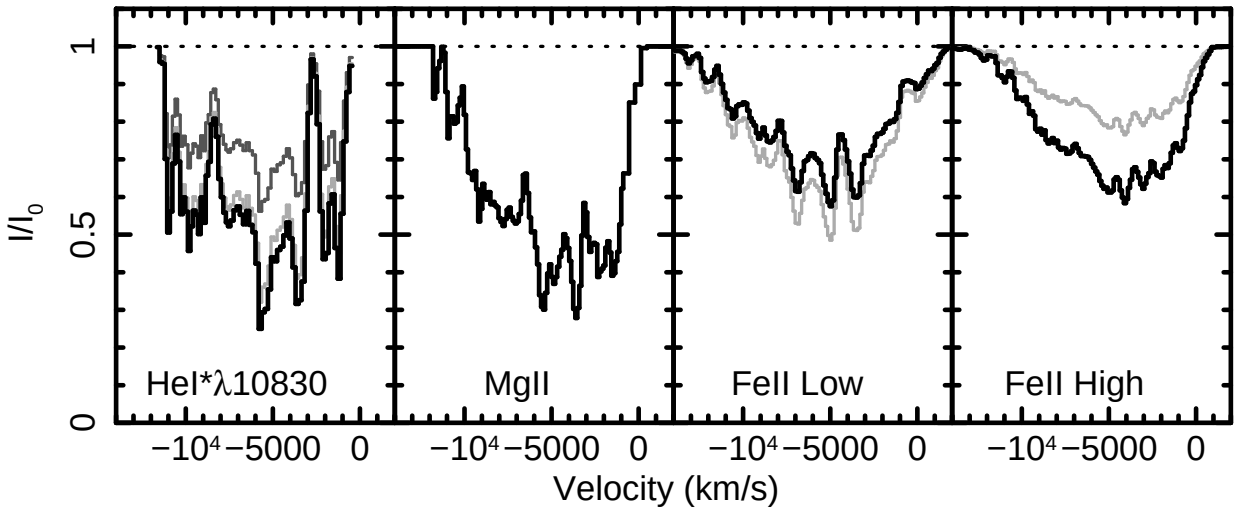

Fig. 9.— The *modeled* ratio I/I_0 for various absorption lines. *Far Left:* The He I*λ10830 ratio. The dark gray line shows the original profile presented in Leighly et al. (2011). The light gray and black lines show the profile after subtracting the galaxy and the galaxy plus torus (Appendix A), respectively. *Middle Left:* The Mg II model ratio from the phenomenological fit model presented in §3.3.3. The velocity is computed using the oscillator-strength-weighted mean wavelength for the doublet. *Right Two Panels:* The Fe II model ratios. The black lines show the ratio from the phenomenological fit model presented in §3.3.3. The gray lines show the levels predicted for the figure-of-merit best fit for the *Cloudy* modeling presented in §4.2. As discussed in §4.3, the right two panels suggest that Fe II Low and High are saturated.

very rapidly at the hydrogen ionization front. This suggests that the spectra of a hypothetical sample of outflows spanning a range of $\log N_H - \log U$ would, if they had sufficient number density to produce Fe II High, generally either have no Fe II absorption, or have saturated Fe II Low and Fe II High.

In any case, it is clear that the Fe^+ apparent columns, like the Mg^+ apparent column, are only lower limits on their respective average columns. Likewise, the best fitting hydrogen column from these apparent columns is only a (very rigorous) lower limit.

An interesting result for BALQSO classifications also emerges from these plots, which suggest that the difference between FeLoBALs, Mg II LoBALs, and HiBALs could be

simply column density relative to the column density of the H II zone. Specifically, if Mg II is present and Fe II is absent, the outflow column density is truncated before the hydrogen ionization front is breached, while the presence of Fe II requires penetration of the hydrogen ionization front. If all low-ionization lines are absent, the outflow column density is truncated before Mg II can populate.

This behavior has a physical explanation. Because photons of only 7.6 eV and 15 eV are sufficient to form, respectively, Mg^{+} from Mg^{0} and Mg^{+2} from Mg^{+}, it is often assumed that Mg^{+} accumulates a significant column density only at depths beyond the hydrogen ionization front, disjoint from the HiBAL-forming gas. However, the 80 eV photon required to form Mg^{+3} from Mg^{+2} means that Mg^{+2} dominates at intermediate depths before the hydrogen ionization front and after the depletion of 80 eV photons, a HiBAL-producing region which includes the He^{+} zone. Recombination onto this Mg^{+2} inevitably produces some Mg^{+}, and because of the high abundance of magnesium (plus the high oscillator strengths of the 2800 Å doublet), this is enough to make an observable, or even strong, line.

The first two ionization potentials of iron (7.9 and 16.2 eV) are quite similar to their magnesium counterparts, but only 30.65 eV is required to form Fe^{+3} (and 54.8 eV to form Fe^{+4}, similar to the 54.4 eV to form He^{+2}). Thus, in the vicinity of the He^{+} zone, where Mg^{+2} dominates over other ionization states, iron is distributed widely between Fe^{+2}, Fe^{+3}, and perhaps some marginal Fe^{+4}, so that much less Fe^{+} forms from recombination. The Fe^{+} column is also distributed amid a greater number of low-energy excitation states than is the Mg^{+} column, with many transitions from those levels, so that observable opacity is even more difficult to develop.

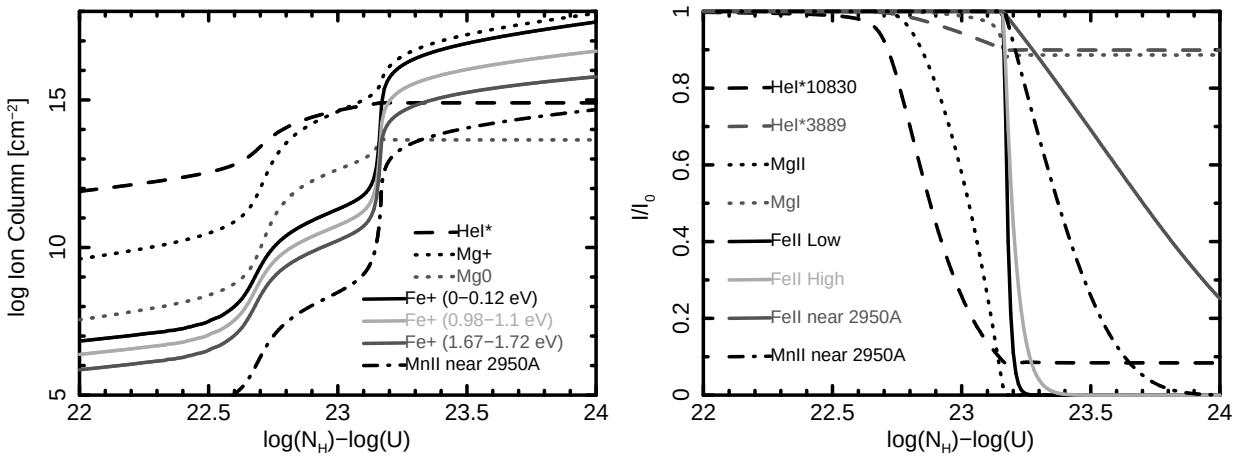

Fig. 10.— Ion columns and resultant I/I_0 ratios as a function of depth into the absorbing gas, from *Cloudy* modeling. *Left:* Predicted log integrated ion column density for $\log U = -1.5$ and $\log n = 7.2$ as a function of $\log N_H - \log U$. *Right:* The same, but with the ion column replaced by the resultant I/I_0 produced by each ion in the line complexes of interest. The absorber is assumed to fully cover the source, for a rectangular absorption profile with a width of $5,000\,\mathrm{km\,s^{-1}}$. These lines show at what depth in the gas the lines will saturate. Among other things, these panels demonstrate the general likelihood of Fe II saturation, the physically distinct regions over which He I* and Fe II produce opacity, and the physical distinction between HiBALs, LoBALs, and FeLoBALs as a matter of gas thickness relative to the hydrogen ionization front. The hydrogen ionization front occurs just short of $\log N_H - \log U = 23.2$.

4.4. Obtaining an Upper Limit on the Column Density

Saturation of Fe II Low and Fe II High (§4.3) means that the best-fitting hydrogen column derived in §4.2 is only a lower limit. But, as discussed in §3.4, there are several relatively shallow Fe II lines just short of 2960Å, corresponding to transitions from the 0.98–1.12 and 1.67–1.71 eV excitation states of Fe II. The 1.7 eV levels are highly excited and thus are expected to have low populations, but their lines have higher oscillator strengths than those of the 1 eV lines at these wavelengths (in our final model, the ratio of 1.7 to 1 eV contribution—measured by integrated τ_{app} from 2852 to 3000 Å—is 1.6 to 1). In addition, there are three important Mn II transitions from excited state levels at 1.17

eV. Manganese is an iron-peak element about 100 times less abundant than iron, but these transitions have high oscillator strengths and moderate excitation (the ratio of Mn II to 1 eV Fe II contribution is 0.94 to 1). Assuming for the moment that these 2960Å lines have the same covering fraction as their Fe II counterparts short of 2800Å, they are sufficiently shallow relative to the covering fraction so as to provide information on the average optical depth, and thus lead to upper limits on column densities. This comes from the fact, demonstrated in Leighly et al. (2011), that for lines absorbing much less than the covering fraction, the apparent optical depth is approximately equal to the average optical depth.

At the hydrogen columns necessary to produce these lines, Cr II and highly excited Fe II also reach significant opacities in various sections of the UV spectrum, and are included in our model. We included all Fe II lines in the bandpass with oscillator strength and air wavelength data from NIST, with lower levels up to 3 eV. Mn II data were likewise taken from NIST, except for a strong ground-state line at 2576Å; this line was missing from NIST, so we included its data from the Kurucz Atomic Line Database[6]. NIST information on Cr II is very incomplete, so we took data for this ion from the Kurucz database, including all lines from < 3 eV with $\log(gf) > -3.0$.

Although *Cloudy* does not output the level-by-level column densities for Mn II and Cr II as it does for Fe II, both Manganese and Chromium are iron-peak elements, so at a given position, the populations of their excited states can be assumed to have the same multiplicative departure from LTE as Fe II does. Thus, we obtained Cr II and Mn II departure coefficients, for each energy level and for each position along the line-of-sight length of the gas, by linearly interpolating over energy between the Fe II departure coefficients of the two nearest Fe II energy levels. Together with the ion fractions and temperatures provided by *Cloudy* incrementally along the length of the gas, we used these

[6]http://www.cfa.harvard.edu/amp/ampdata/kurucz23/sekur.html

to calculate the net column densities of energy states as the integrals over length of the product of departure coefficient and LTE density.

We computed these ion columns for a range of hydrogen columns. Levels from excited states greater than ~ 2 eV above ground are extremely depleted by departure from LTE, but this effect has minimal impact on the partition function due to the high energies at which it becomes significant. So for the ~ 2960Å lines (which are all from levels below 2 eV), the columns densities are near LTE (Fig. 11). We investigated density dependence and found it to be insignificant. We also tested Ti II, but this ion turned out to have virtually no opacity in our bandpass, so we ignored it.

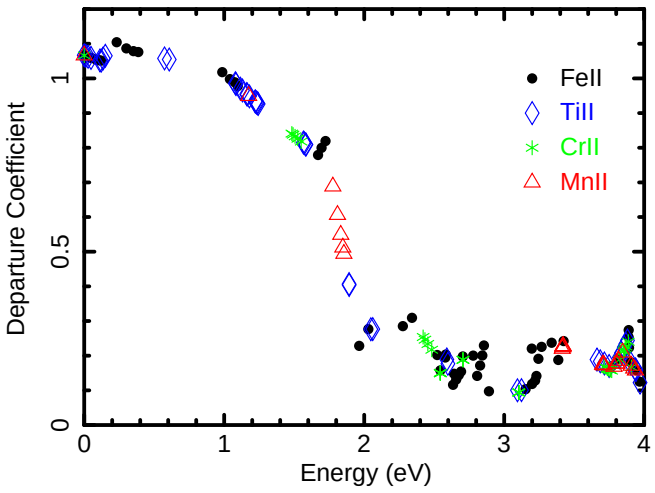

Fig. 11.— Aggregate departure coefficient (i.e., our integrated non-LTE column density divided by our integrated LTE column density) as a function of energy level above ground, for several once-ionized iron-peak elements. Depletion by non-LTE effects rapidly becomes insignificant below ~ 2 eV.

Using the continua and He I* templates described in §3, we constructed the predicted spectrum for a range of $\log(N_H) - \log(U)$ at $\log n = 7.2$ and $\log U = -1.5$. Average column densities for each ion and energy level, obtained from *Cloudy* parameter space as described above, were translated into average optical depths for each corresponding line using Equation 2, which were converted to true optical depths using $\tau_{avg} = C_f \, \tau_{true}$. These

true optical depths were then converted to into the observed I/I_0 using Equation 5. We used a covering fraction C_f of 0.25, corresponding to the average fraction (weighted by the inverse of the observed flux's Poisson variance) of the continuum absorbed between 2500 and 2620 Å, the range over which Fe II Low is *completely* saturated at high hydrogen columns.

By the time $\log(N_H) - \log(U)$ reaches 23.4, the model absorption is deeper than the spectrum by a substantial amount (corresponding to at least $\sim$ twice the typical systematic errors implied by the few wavelengths where our continua models drop below the spectrum) for the unabsorbed data between $\sim$ 2852 and $\sim$ 2890Å, as well as for a substantial fraction of the longward absorption features. In fact, at this column density, the $\sim$ 2852 to $\sim$ 2890Å criterion was very nearly met for covering fractions as low as $\sim$ 0.1. A model spectrum for this column is shown in the lower-left panel of Fig. 3, which was made using a velocity-constant $C_f = 0.25$ for iron-peak absorbers. We used $C_f = 0.58$ for magnesium absorbers, the weighted average fraction of the continuum absorbed between 2690 and 2788 Å, the range over which Mg II is completely saturated. The ion column densities for this upper limit are tabulated in the last row of Table 2. The contributions of each line to the composite Fe II (0.98–1.12), Fe II (1.67–2.89 eV), Mn II, and Cr II average optical depths at this hydrogen column are shown in the bottom panels of Fig. 5.

This upper limit model also exemplifies the manner in which saturation and partial covering can equalize the Fe II Low and Fe II High absorption complexes, as well as yield the observed profile of Mg II. It shows that the covering fraction for Mg II is more than twice that of the broad Fe II complexes, a subject which we discuss further in §5.1. That said, this model is far from being a complete physical picture; for example, it yields too much absorption from Mn II and the upper levels of Fe II at short wavelengths, fits the 2960Å lines poorly, and yields too much absorption between 2852 and 2890Å. Therefore, we

explore inhomogeneous models in the next section.

4.5. A Possible Model of Inhomogeneity

Despite the fact that our models reproduce the spectra reasonably well, previously-discussed regions of poor fit in the lower (§4.2, §4.3) and upper (§4.4) limit spectral models, which remain problematic in models with intermediate hydrogen columns, imply that the real situation may be more complicated. Our assumption that the absorption profiles of once-ionized iron-peak elements and Mg II are the same as that for He I* probably contributes to the inconsistencies, as does our assumption of a velocity-constant covering fraction. In addition, the absorber could be inhomogeneous, so that the apparent step-function covering fraction (i.e., that obtained by assuming homogeneity) will be a convolution of the line strength and the spatial dependence of gas column.

The plausible large number of degrees of freedom, significant line blending, and poor signal-to-noise ratio mean that no unique solution is possible. However, as shown in this section, further examination of the data can lead us to a possibly plausible, albeit ad hoc, phenomenological, and unconstrainable, physical picture composed of three outflow components. Our purpose here is not to present a final model, but to propose a possible physical picture and determine the specific weak points of our homogeneous-model kinematic constraints.

We broke the template profile into three velocity pieces with different opacities and covering fractions. First, an intermediate-velocity narrow Gaussian centered near $-3,300$ km s^{-1} is suggested by the high-excitation Fe II and Mn II near 2960Å, and probably has high opacity (to produce these underpopulated lines) and low covering fraction (since these lines are not deep). Second, a low-velocity component between $\sim -2,300$ and

$-1,000\,\mathrm{km\,s^{-1}}$ is required to model the deepest part of ground-state Fe II and Mg II; this component cannot have high opacity (because it would produced too much absorption from 2631Å Fe II, an objectionable property of the upper limit as seen in Fig. 3) but must have high covering fraction (since Mg II is deep). The final, high velocity component, between $-11,000$ and $-4,000\,\mathrm{km\,s^{-1}}$, is adapted from the He Iλ10830 profile; this component should have intermediate optical depth and intermediate covering fraction, as it represents the bulk of the template fit. That is, the modifications that we are making in this analysis influence most heavily the lower velocity components.

To model the composite absorption, we used an inhomogeneous covering model which models the optical depth τ as a power law (Arav et al. 2005; Sabra & Hamann 2005), parameterized by τ_{max} and power law index a because, unlike the step-function partial covering, the composite I/I_0 is a product of the I/I_0 for the three components. We varied the power law slope and maximum opacity by hand, and applied the resulting optical depth profile to the continuum. The resulting model is shown in the lower-right panel of Fig. 3. The parameters are only loosely constrained by the data, so this is not a formal fit, but rather a plausible model. However, some illuminating trends emerge. First, as expected, for the $-3,200\,\mathrm{km\,s^{-1}}$ component, τ_{max} has to be large to reach the substantial optical depths required to produce the lines near 2960Å, but a also has to be large to yield a sufficiently low covering fraction so that the lines near 2600 and 2700Å are not too deep. Second, the low-velocity component has to have the smallest value of a to yield a large enough covering fraction to produce the deep low-velocity component of Mg II. Finally, the high-velocity component has to have low-intermediate values of a and τ_{max} to fill in the remaining Mg II.

This inhomogeneous model explains the 2960Å features better than any other model we devised. And since the very high opacity is limited to the $-3,200\,\mathrm{km\,s^{-1}}$ component, it does not produce too much opacity between 2600 and 2631Å. That said, this model

produces insufficient Fe II High opacity between 2650 and 2700Å, while also producing too much higher velocity Fe II Low. This might occur if the distribution is something different than a power law.

This model suggests that the outflow's most important inhomogeneity is a narrow component near $-3,200\,\mathrm{km\,s^{-1}}$ that has a low covering fraction and very high gas column (equivalently, high optical depth), primarily evidenced by the $\sim$ 2960Å lines that appeared between the SDSS observation in 2005 and this KPNO observation in 2011. If this component is part of the main outflow, it should have a similar distance from the central engine. So, perhaps the inhomogeneity consists of new higher density condensations that have developed inside the lower optical depth, higher covering fraction outflow. A higher density in the condensations would yield a lower ionization parameter, but Mg II and Fe II ionic column density contours run parallel to the ionization parameter (e.g., Fig. 7), so the ions present would not necessarily change much.

Is this component really part of the main outflow? There is some, rather weak, evidence in favor of this hypothesis. Certainly, the presence of high-excitation iron in the condensations requires a high density, and therefore an absorption radius, like that of the broad line outflow, rather close to the nucleus (§5.2). Furthermore, this component varies on relatively short time scales (i.e., between the SDSS observation in 2005 and the KPNO observation in 2011), and timescales can be shorter closer to the nucleus due to higher densities / shorter recombination times, or shorter crossing times for clouds moving across the line of sight (e.g., Capellupo et al. 2011, and references therein). Furthermore, as discussed in §3.4, there are some hints that the velocity of these new cores was predicted, to some extent, by the structure of the He I* BALs in older spectra, when the cores were not observed.

This analysis introduces a note of caution into our constraints; the presence of dense,

low covering fraction inhomogeneities throws some uncertainty into our assumption that the spatial gas distribution can be approximated as a step function. In particular, additional mass may be hidden in such cores, which we do not consider in the following section because it cannot be constrained with the available data; for example, the new lines appeared sometime between the 2005 and 2011, so the upper limit on density obtained from Balmer constraints in Leighly et al. (2011) (using the 2005 spectrum) may not apply to the cores.

4.6. A Density Lower Limit

To obtain a lower limit on the characteristic number density in the BAL flow, we investigated the dependence of Fe^+ level populations on density and $\log(N_H) - \log(U)$ for fixed $\log U = -1.5$. We first looked at the dependence for Fe II Low, finding that $\log n > 5.1$ is required to produce the measured column density. We then looked at the density dependence of levels between 0.98 and 1.72 eV, i.e, levels that contribute to both Fe II High and to the Fe II near 2960Å. For column densities up to $\log(N_H) - log(U) = 24$, we do not populate the levels near 1 eV and 1.7 eV sufficiently unless the density is greater than $\log n = 5.5$ and $\log n = 6.2$, respectively. It was the lack of the broad component absorption in the 1.7 eV levels that contributed to our column density upper limit of $\log(N_H) - log(U) = 23.4$ (§4.4), so we instead rely on the 1 eV level constraint, yielding $\log n = 5.5$ as our conservative density lower limit.

4.7. Kinematic Constraints

In this section, we describe new constraints on the kinetic parameters of the outflow. We followed the standard methodology, which was described and used on this object in Leighly et al. (2011). As detailed in Leighly et al. (2011), we used a characteristic

column-weighted velocity of $-5400\,\mathrm{km\,s^{-1}}$, an assumed global covering fraction $\Omega = 0.2$, and a matter-to-radiation conversion efficiency of 10%. We made one small change, however; due to a more careful dereddening presented in this paper, the estimated optical flux is larger by 20%. This in turn increases the estimated black hole mass by 4%, to $8.5 \times 10^8\,M_\odot$, and the bolometric luminosity became $6.3 \times 10^{46}\,\mathrm{erg\,s^{-1}}$ (obtained by integrating over the *Cloudy* model continuum scaled to the dereddened optical flux).

We investigated the kinematic properties of the BAL-producing outflow, characterized by broad Fe II Low, Fe II High, Mg II, and He I*, ignoring the kinematics of poorly constrained dense-core inhomogeneities posited in the preceding section. In Leighly et al.

Table 3. Kinematic Limits for the Broad Outflow

Parameter	Weakest Outflow	Strongest Outflow
log Ionization Parameter	−1.5	−1.5
log Density [$\mathrm{cm^{-3}}$]	8.0	5.5
$\log N_H - \log U$	23.18	23.4
$\log N_H$[a]	21.68	21.9
Radius [pc]	7.2	127
Mass Flux[a] [$\mathrm{M_\odot\,yr^{-1}}$]	10.7	315
Kinetic Luminosity[a] [$10^{44}\,\mathrm{erg\,s^{-1}}$]	0.99	28.9
Kinetic Luminosity[a] / Bolometric Luminosity	0.16%	4.5%
Outflow Rate[a] / Accretion Rate[b]	0.96	28.3

[a]Assuming global covering fraction $\Omega = 0.2$.

[b]Assuming an accretion efficiency of 10%.

(2011), we had to assume acceleration by radiative line driving (which yielded a density lower limit) in order to constrain kinematic properties; the additional information provided here by Fe II has allowed us to lift that assumption. §4.2, §4.4, and §4.6, along with a density maximum obtained from upper limits on Balmer absorption in Leighly et al. (2011), constrained the gas parameters in the main outflow to the following ranges: $\log U = -1.5$, $5.5 \leq \log n \leq 8$, $23.18 \leq \log N_H - \log U \leq 23.4$, and correspondingly $21.68 \leq \log N_H \leq 21.9$. Choosing combinations of these limits that extremize the outflow's power and radius, we constrained kinematic parameters to the following ranges: radius (distance from the central engine) between 7.2 and 127 parsecs, mass flux between 10.7 and 315 $M_\odot\,yr^{-1}$, and kinetic luminosity between 1.0×10^{44} and 29×10^{44} erg s^{-1}. This range of kinetic luminosity is between 0.16% and 4.5% of the bolometric luminosity, and the ratio of mass flux to accretion rate is between 0.96 and 28.3. These constraints are summarized in Table 3.

Our results depend somewhat on the shape of the input SED, which we cannot estimate for FBQS J1151+3822; the UV continuum appears to be reddened, and there is no X-ray detection. We used a generic AGN continuum from Korista et al. (1997)[7], which we have used with success on various objects, and on this object in Leighly et al. (2011). But to investigate the influence of SED choice, we have performed some simulations using the much softer SED that Hamann et al. (2013) use. This SED would yield an inferred distance from the continuum smaller by $\sim 28\%$; this is negligible considering the range of uncertainties. The softer SED is, however, so weak in X-rays that it produces a cool partially ionized zone, increasing the upper limit on $\log(N_H) - \log(U)$ to greater than 24. Such a large amount of material (i.e., ~ 10 times the Stromgren sphere thickness) might be difficult to accelerate. At any rate, given that we have no direct information about the shape of the SED, and for continuity with our previous paper, we assumed the generic

[7]The *Cloudy* command for this continuum is "AGN Kirk."

Korista et al. (1997) continuum.

5. Discussion

5.1. Inhomogeneous Absorption in FBQS J1151+3822

The simplest interpretation of partial covering, that part of the continuum source is covered uniformly while the remainder is uncovered, may not be generally valid. Rather, the distribution of hydrogen column can be inhomogeneous across the line of sight. Hamann et al. (2001) propose an absorber of large/low-density blobs that allow for sufficient opacity from strong (but not weak) lines to be observed, along with small/higher-density cores that allow for sufficient opacity from weak lines. In this model, the observed step-function covering fractions are larger for stronger lines, matching their observations. Lines with small oscillator strengths and/or low species abundance only sample the smaller cores of dense gas, which have less overall coverage of the source. That is, weak lines will show smaller covering fractions when one applies the step-function covering fraction model to a very inhomogeneous gas.

Aside from that, lines that arise in different physical conditions can also have different covering fractions. A related idea, similar to the scenario proposed by Voit et al. (1993), might have radiation pressure ablating extended lower-density/higher-ionization gas from dense cores; this picture has the advantage that it could also explain the extension of higher-ionization lines to larger velocities observed in some objects.

Arav et al. (2005, 2008) have explored some simple inhomogeneous distributions, such as a power law distribution in one spatial dimension. In Arav et al. (2008), homogeneous and inhomogeneous fits yield ionic columns within 25% of each other, and similar parity between methods was seen in Leighly et al. (2011). However, extreme power laws, not to

mention more complex distributions, could behave less like a step function distribution, and there appears to be little observational evidence in the literature to suggest a universal distribution.

As discussed in §4.5, inhomogeneous partial covering is required to explain the spectrum of FBQS J1151+3822. Expressed in terms of a geometrical covering fraction, we find that the spectrum can be fit best if the line-of-sight covering fractions around ~ 0.25 for Fe II, increasing to ~ 0.5 for He I* and ~ 0.6 for Mg II (e.g., Fig. 3, Fig. 9). In addition, the lowest opacity lines, exemplified by the new, relatively narrow lines observed near 2960Å, may have an even lower covering fraction in the vicinity of ~ 0.1 to ~ 0.2.

We can use this information, combined with the information in Fig. 10, to crudely map the column density to the covering fraction. For example, we know that gas with $\log N_H - \log U \approx 23.2$, where Fe II saturates, must cover less than $\sim 50\%$ of the continuum emission source, otherwise the Fe II lines would be as deep as the He I*λ10830 and Mg II lines. Likewise, gas with $\log N_H - \log U \geq 23.5$ must cover less than $\sim 30\%$ of the continuum emission source, or the lines near 2960Å would be deeper. Information from higher-ionization lines, such as Si IV, which saturates at $\log N_H - \log U \approx 22.8$, and C IV, which saturates at $\log N_H - \log U \approx 22$, would fill in information for smaller column densities.

With more line species, a distribution of column density as a function of effective covering fraction could be made, under the assumption of constant density, that could potentially be used to build a model of inhomogeneity. This also brings out a under-appreciated difficulty in analyzing BALQSO spectra; that is, if the covering fraction can be measured using two lines (e.g., as was done in Leighly et al. 2011), that covering fraction often cannot be assumed to apply to other lines less amenable to covering fraction analysis (e.g., if the gas is non-uniform *and* lines are not equally strong, or do not form in equal

amounts in identical conditions).

Finally, it is interesting that Mg IIλ2800 has, in our best estimates, a covering fraction somewhat higher than that of He I*λ10830 (~ 0.6 to ~ 0.5). As discussed in Leighly et al. (2011) and elsewhere, the continuum emission region is expected to be extended, with the longer wavelength continuum produced over a more extended area. For example, for $M_{BH} = 8.5 \times 10^8\,\mathrm{M}_\odot$ and $\dot{M} = 11.1\,\mathrm{M}_\odot\,\mathrm{yr}^{-1}$, the 2800Å and 10830Å regions are expected to have peak emission at 0.008 and 0.047 pc, respectively, from the center, based on a sum-of-blackbodies accretion disk model (e.g., Frank et al. 2002). Thus, it is possible that the projected size of the absorber is large compared with the 2800Å emitting region, and slightly smaller compared with the 10830Å emitting region.

5.2. Comparison with Other FeLoBALs

The unambiguous detection of Fe II absorption reclassifies FBQS J1151+3822 as an FeLoBAL. With $z = 0.3344$ and $M_V = -25.5$, it is presently the second-nearest and second-brightest example of this class, after Mrk 231. Detailed analyses of Mg II, Fe II and He I* in FeLoBALs have been presented by other authors. However, because this type of analysis is very difficult, as a consequence of severe blending and the large number of lines that may be present, it has been applied to only a handful of objects. Here we discuss those results, and compare with our results from FBQS J1151+3822. This comparison is summarized in Table 4, and the spectra of several objects are presented in Fig. 12.

In many cases, the authors used a template method to analyze the data, like we did; they generally developed the template from a narrow, unblended line from e.g., Mg I, Fe II, or Zn II (de Kool et al. 2001, 2002b,a). In some objects, the lines were sufficiently narrow and unblended that a direct line-fitting approach could be used (Arav et al. 2008;

Moe et al. 2009; Dunn et al. 2010).

In some cases, the presence of lines determined to originate in well-populated, highly-excited Fe II led the authors to conclude that the gas is dense, with densities greater than, e.g., $\log n_H = 10^6\,\mathrm{cm}^{-2}$, and the absorption region compact, lying within e.g., 1 pc from the central engine (Wampler et al. 1995; de Kool et al. 2002b,a). In other cases, the high-excitation Fe II lines are absent, and the low-excitation Fe II displays ratios that suggested low densities, and therefore large distances between the absorbing gas and the central engine, e.g., hundreds to thousands of parsecs (de Kool et al. 2001, 2002a; Korista et al. 2008; Moe et al. 2009; Dunn et al. 2010). In one case, the absorption was separated into two kinematic components, with the high-velocity lines consistent with high-density gas, and the low-velocity lines consistent with low-density gas (de Kool et al. 2002a).

Several authors concluded that Fe II is produced in a thin layer near the hydrogen ionization front (Wampler et al. 1995; de Kool et al. 2001; Korista et al. 2008). Some speculated that the width of that region could be broadened by the presence of dust (de Kool et al. 2001), while in other cases dust is ruled out by the absence of strong neutral absorption (de Kool et al. 2002b). Some have commented on the fact that Mg II is deeper than Fe II, indicating a higher covering fraction (Wampler et al. 1995), while others have noted, like we have, that the most prominent Fe II lines are saturated (de Kool et al. 2001).

Fig. 12 shows a comparison of our KPNO spectrum of FBQS J1151+3822 with the SDSS spectra of FBQS J1044+3656, SDSS J0318−0600, FBQS J1214+2803, and FBQS J0840+3633, and a spectrum of Q J0059+2735 previously published by Weymann et al. (1991). On this plot we mark the extent of lines from various ions including Mg II, Mg I, and Fe II, breaking the Fe II into low-excitation Fe II (rest wavelengths 2586 – 2631Å and 2327 – 2411Å, lower level energies 0 – 0.12 eV), high-opacity high-excitation

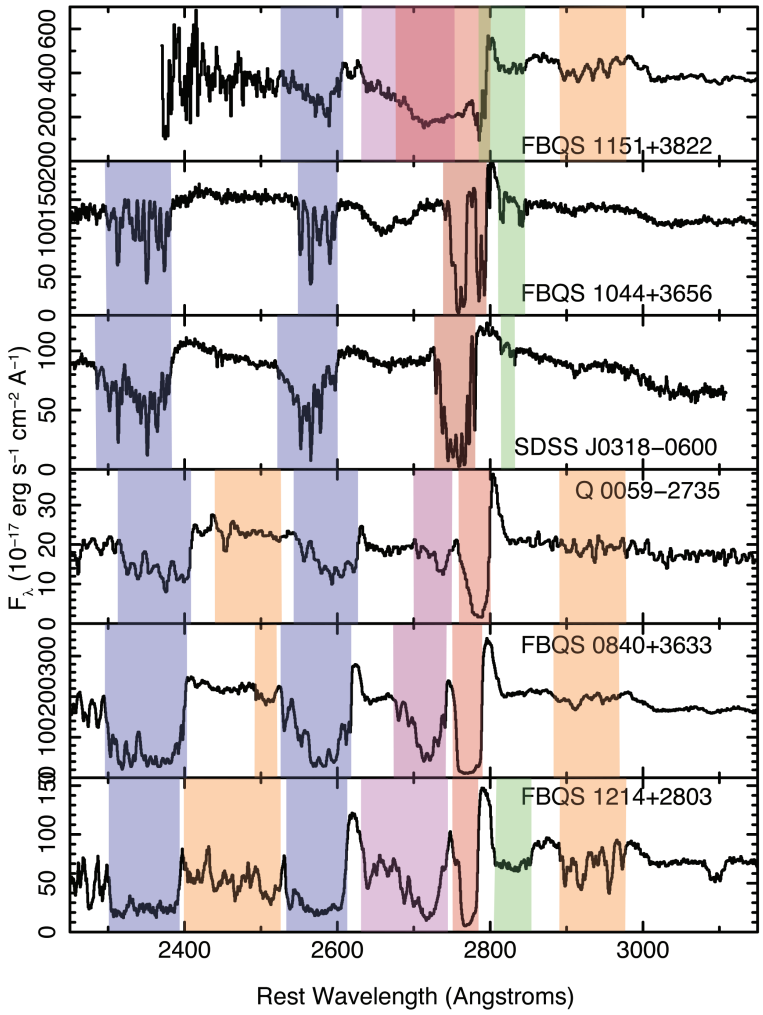

Fig. 12.— FBQS J1151−3822 in comparison with spectra of other bright, well-studied FeLoBALs, including FBQS J1044+3656 (de Kool et al. 2001), SDSS J0318−0600 (Dunn et al. 2010), Q J0059−2735 (Wampler et al. 1995), FBQS J0840+3633 (de Kool et al. 2002a), and FBQS J1214+2803 (e.g., de Kool et al. 2002b). Note that the Q J0059−2735 spectrum is a lower-resolution, lower signal-to-noise ratio spectrum published by Weymann et al. (1991), and thus some of the low-equivalent-width line identifications are uncertain. Shaded regions denote the extent of various absorption lines, and absorption-line classes, as follows: red: Mg II$\lambda\lambda$2796, 2803, observed near 2770Å; green: Mg Iλ2852, observed near 2830Å; blue: low-excitation Fe II, observed between $\sim$ 2300 and $\sim$ 2400Å and between $\sim$ 2530 and $\sim$ 2600Å; purple: high opacity high-excitation Fe II, observed between $\sim$ 2650 and $\sim$ 2750Å; orange: low-opacity high-excitation Fe II, observed between $\sim$ 2900 and $\sim$ 2970Å, and between $\sim$ 2400Å and $\sim$ 2520Å . Objects with low-density absorbing gas, including FBQS J1044+3656 and SDSS J0318−0600, can be easily distinguished by eye (by their lack of high-excitation Fe II emission) from objects dominated by higher density gas, including FBQS J1151+3822, Q J0059−2735, FBQS J0840+3633 and FBQS J1214+2803.

Fe II (2693 – 2773Å; 0.98 – 1.1 eV), and low-opacity high-excitation Fe II (2372 – 2641Å, 2944 – 3002Å; 1 – 3 eV, plus 1.17 eV Mn II).

A general sense of physical conditions in the absorbing gas can be gained by simply examining Fig. 12 to see which types of Fe II lines are present and how deep they are. For example, FBQS J1044+3822 has no Fe II High, and therefore it can be concluded on-sight that the density is low and excited states are underpopulated. SDSS J0318−0600 is similar. FBQS J1214+2803, on the other hand, shows absorption lines from ions with very high excitation and high column density, indicating high density. The same goes for FBQS J1151+3822, which may also have the broadest absorption features.

Table 4 gives estimated densities and distances of the absorber from the central continuum source for various FeLoBALs, as given in the referenced publications. These trends substantiate our assertions from the figure; the two objects that lack Fe II absorption from highly excited iron ions have low estimated densities, and the distances from the central engine are large, while the objects with strong high-excitation Fe II have high estimated densities, and the distances from the central engine are small. Note that it is somewhat difficult to compare the distances directly, since these objects have a range of intrinsic luminosities. As will be discussed in §5.3, it would be easier to compare distances if they were scaled by a characteristic radius that accounts for the variations in intrinsic luminosity. Nevertheless, here we use absolute distance in parsecs for comparison with previous work.

de Kool et al. (2002a) have already suggested that there are, among Fe II absorbers, perhaps two classes with different characteristics: one with lines consisting of "one or several narrow components, sometimes blended together into wider structures that are formed in a low-density gas at a large distance (0.1–10 kpc) from the nucleus," and another with broader lines and broader substructure with densities "higher by several orders of

Table 4. FeLoBAL Parameter Comparison

Target	Inferred Density [cm^{-3}]	Inferred Distance [pc]	References
Q0059−2735	10^6–$10^{8.5}$	0.6–40	Wampler et al. (1995)
FBQS J1044+3656	$\sim 4 \times 10^3$	700	de Kool et al. (2001)
FBQS J1214+2803	$> 10^6$	1–30	de Kool et al. (2002b)
FBQS J0840+3633[a]	10^9 – 3×10^{10}	1–30	de Kool et al. (2002a)
	< 500	~ 230	
QSO J2359−1241	$10^{4.4}$	3,000	Korista et al. (2008)
SDSS J0838+2955	$10^{3.75}$	3,300	Moe et al. (2009)
SDSS J0318−0600	$10^{3.3}$	6,000-17,000	Dunn et al. (2010)
FBQS J1151+3822	$10^{5.5}$–10^8	7.2–127	this paper

[a]de Kool et al. (2002a) report that there are two kinematically-distinguishable components in this object that are characterized by different densities and distances from the central engine.

magnitude [. . .] best explained if they are 1000 times closer to the nucleus, 0.1–10 pc." The radius constraints for the FBQS J1151+3822 outflow , at 7.2 to 127 pc, straddle the gap between de Kool's classes. This could in part be because our constraints are very conservative, because de Kool et al.'s analysis was based on only a few targets, or because they did not account for differing black hole masses.

Moreover, our *Cloudy* models suggest that the bimodality de Kool et al. see in FeLoBAL spectra is not, in fact, *necessarily* accompanied by a physical bimodality. Fig. 13 shows I/I_0 for Fe II Low and Fe II High as a function of density and $\log(N_H) - \log(U)$ for an example ionization parameter of $\log U = -1.5$ and $\Delta V = 5,000\,\mathrm{km\,s^{-1}}$. Examining this figure, we see the expected decrease in I/I_0 at the hydrogen ionization front near $\log(N_H) - \log(U) = 23.2$. But we also see that while Fe II Low absorption is strong enough to saturate the line at all densities, Fe II High saturates only for densities higher than $\log(n) \sim 5.5$, and that Fe II High goes from being negligible to saturated over a relatively small range in density.

This behavior, plus the rapid transition to saturation present just past the hydrogen ionization front, means that for a population of objects with a flat or unimodal distribution of characteristic densities, one is still likely to see either objects with Fe II Low alone (low density objects with hundreds-pc to kpc scale absorbing regions) or objects with both strong or saturated Fe II Low and Fe II High (high density objects with pc to tens-of-pc scale absorbing regions). Thus, we find the bimodality of Fe II absorption in quasars that de Kool et al. (2002a) observed can be reproduced from the astrophysics of Fe II absorption, without recourse to a physically bimodal population of FeLoBAL quasars.

Finally, we note that this behavior of Fe II could bias target selection in the near-UV. Density can be estimated with precision if ground and excited state transitions of iron are present. Detailed analysis is easier and less ambiguous when lines are rather narrow

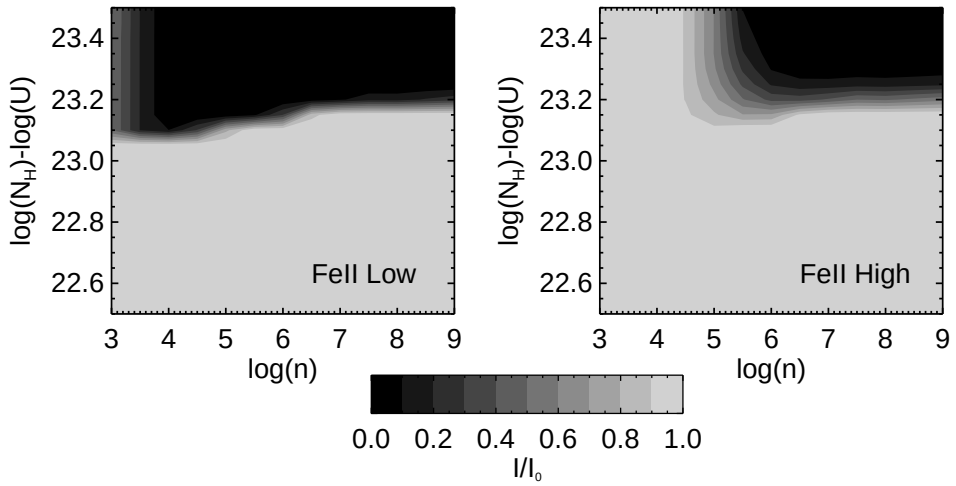

Fig. 13.— Predicted I/I_0 for Fe II Low (transitions with E_{lower} near 0 eV, between 2500 and 2650Å) and Fe II High (transitions with E_{lower} near 1 eV, between 2650 and 2800Å) for $\log U = -1.5$ as a function $\log n$ and $\log N_H - \log U$. The absorber is assumed to fully cover the source and the absorption profile is rectangular with a width of $5,000\,\mathrm{km\,s^{-1}}$. These contours illustrate the rapid onset of Fe II absorption near the hydrogen ionization front, and the sharp density dependence of Fe II High.

and unblended. Gas with ions populated to higher levels will produce more lines, causing more blending. So objects with lower-density gas and therefore fewer lines would present spectra more amenable to analysis. Thus, objects with low-density gas, and therefore kiloparsec-scale outflows, might be preferentially selected.

5.3. Kinematic Comparison to Other BALQSOs

Recently, some authors have made very speculative statements about locations of the BAL gas (e.g., Borguet et al. 2013; Arav et al. 2013). While perhaps implicitly allowing for a population of outflows ~ 100 pc away from the continuum source (e.g., Borguet et al. 2013), these authors strongly emphasize powerful outflows at kiloparsec scales, with ~ 100 pc seeming like a rather strong minimum. For example, Arav et al. (2013), who use O IV/O IV* as a density diagnostic, say that their absorption radii are "4+ orders of

magnitude farther away than the assumed acceleration region (0.03 – 0.1 pc) of line-driven winds in quasars. This result is consistent with almost all the distances reported for AGN outflows in the literature."

In contrast, we find that the BAL outflow in FBQS J1151+3822 is located, conservatively, somewhere between 7.2 and 127 pc from the continuum source; our upper limit overlaps only with the extreme end of the Arav group's range of objects, and most of our allowed radii range is on the tens-of-parsecs scale. Does FBQS J1151+3822 then have an unusually low-radius BAL outflow?

We think not; rather, we hypothesize that the many AGN outflows in the literature could be subject to a selection bias. These quasars were chosen because their spectra contain lines from ground and excited state ions with ratios that can be used to estimate the density. As we will show, this selection preferentially picks out objects with low densities and therefore large absorption radii.

Consider, for example, S IVλ1063 and S IV*λ1073 (Leighly et al. 2009; Borguet et al. 2013). These two lines represent transitions from the $^2P^0\ J = 1/2$ ground state and the $^2P^0\ J = 3/2$ excited state. The critical density for the excited state line for a typical nebular temperature of $10,000\,\mathrm{K}$ is $n_{crit} = 4.2 \times 10^4\,\mathrm{cm}^{-3}$. The density ratio of the first excited state to the ground state will be equal to the column density ratio, assuming uniform gas conditions (Fig.14). Similar plots are found in Borguet et al. (2013) for S IV, for O IV in Arav et al. (2013), for Fe II in Korista et al. (2008), and for Si II in Dunn et al. (2010).

To examine the useful range of density over which this line ratio can be used, we consider some limiting cases. We ignore partial covering, which can add considerable uncertainty to the line measurement. As density increases, the excited state will become more populated. We assume that we can measure absorber populations when their observed lines are at least as deep as $I/I_0(v) = 0.95$, and at least as shallow as $I/I_0(v) = 0.05$.

Likewise, the highest density we can measure with a reasonable degree of accuracy requires that neither line be saturated, and therefore they should have different values of I/I_0. Since the excited state can have a higher population than the ground state for this pair of transitions, we assume that it has $I/I_0(v) = 0.05$ when the ground state has $I/I_0(v) = 0.1$. Using these two limits shows that the useful density range for this line is between $4.5 \times 10^2\,\mathrm{cm}^{-3}$ and $1.7 \times 10^5\,\mathrm{cm}^{-3}$, or between 0.01 and 3 times the critical density. The precision with which these measurements can be made depends on the quality of the data; nevertheless, it is clear that any particular density diagnostic works best in the vicinity of the critical density.

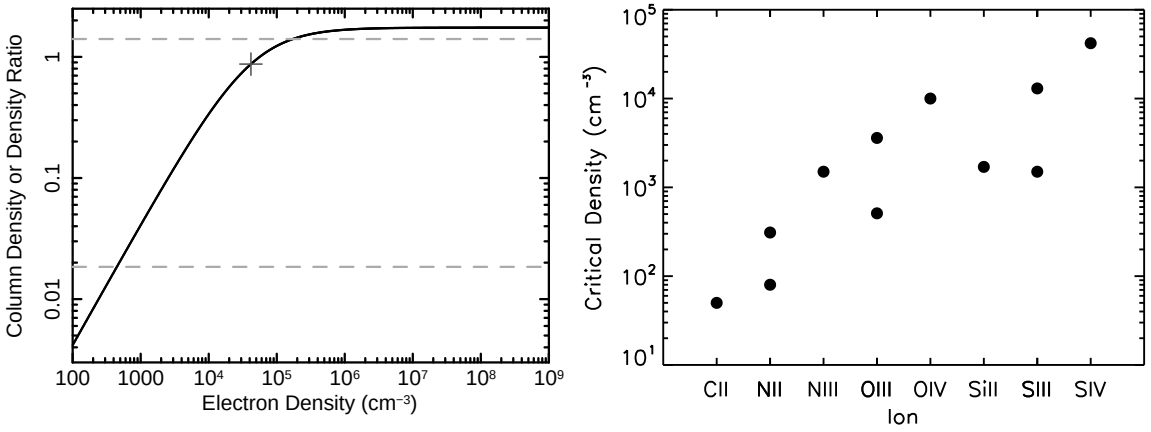

Fig. 14.— *Left:* The predicted ratio of density of the excited state S IVλ1073 to the density of the ground state S IVλ1063, calculated assuming a temperature of $10,000\,\mathrm{K}$. The dark gray plus sign denotes the critical density ($4.2 \times 10^4\,\mathrm{cm}^{-3}$). The dashed lines show the plausible upper and lower limits for secure ratio measurements (see text for details). These imply that S IV can be used to measure densities between $4.5 \times 10^2\,\mathrm{cm}^{-3}$ and $1.7 \times 10^5\,\mathrm{cm}^{-3}$, or between 0.01 and 3 times the critical density, suggesting a selection bias inherent in using density-sensitive lines. *Right:* Critical densities for common ions. Ions with a single value of critical density have two levels of fine structure in their ground state. Ions with two values have three levels, hence different values of critical density for each of the two excited states.

Fig. 14 shows the critical densities for many of the most common ions with ground-state fine structure that are seen in BAL outflows. The first problem is that ions with three-level

ground states with $J = 0, 1, 2$ have two critical densities, from the $J = 1$ and $J = 2$ levels. These critical densities can be dramatically different, making these lines particularly difficult to analyze since the separation of the lines is small. This issue was discussed for metastable C III*λ1175 observed in NGC 3783 by Gabel et al. (2005). The second problem is that the density-sensitive lines have a limited range of critical densities, all less than that of S IV. Since the S IV can be used to securely measure densities less than $\sim 1.7 \times 10^5\,\mathrm{cm}^{-2}$, as we have shown above, selecting objects with lines amenable to this kind of analysis pre-selects objects that have low outflow densities.

How does this selection impact the inferred radii? The radius is linked to the density through the ionization parameter and the ionizing flux. For a range of ionization parameters and densities, we can compute the radius for a fixed number of ionizing photons. It first makes sense to normalize the radius by dividing by a characteristic radius, to account for the wide range of possible AGN luminosities. We normalize by R_{TK}, the reverberation mapping radius of the K-band photometry, which can be taken to be the radius of the torus. R_{TK} is given by Kishimoto et al. (2011) as $R_{TK} = 0.47(6\nu L_\nu(5500\text{Å})/10^{46}\,\mathrm{erg\,s}^{-1})^{1/2}\,\mathrm{pc}$, where $6\nu L\nu(5500\text{Å})$ is a surrogate for the UV luminosity. For FBQS J1151+3822, $R_{TK} = 0.82\,\mathrm{pc}$, for the low-luminosity BALQSO WPVS 007 (Leighly et al. 2009), $R_{TK} \approx 0.023\,\mathrm{pc}$, and for HE0238−1904 (Arav et al. 2013), $R_{TK} \approx 1.3\,\mathrm{pc}$. Thus, for typical BALQSOs, R_{TK} is on the order of a parsec.

We plot the inferred outflow radii normalized to R_{TK} in Fig. 15 as a function of a typical range of ionization parameters and density. We also mark $1.7 \times 10^5\,\mathrm{cm}^{-3}$, the plausible upper limit of density obtainable using the density-sensitive lines. This shows that, for a typical ionization parameter of $\log U = -1.5$, no distances smaller than $R_{out}/R_{TK} = 210$ would be measurable. That value decreases to 67 for a higher ionization parameter of $\log U = -0.5$ and increases to 667 for a lower ionization parameter of $\log U = -2.5$. More

typical densities reported in the literature, e.g., $\log n \approx 4$, yield a lower limit on R_{out}/R_{TK} between 275 and 2750 pc, i.e., very far from the central engine. Since radius enters linearly in the equation for kinetic luminosity (e.g., Eq 1 in Arav et al. 2013), a large radius inevitably produces a large kinetic luminosity.

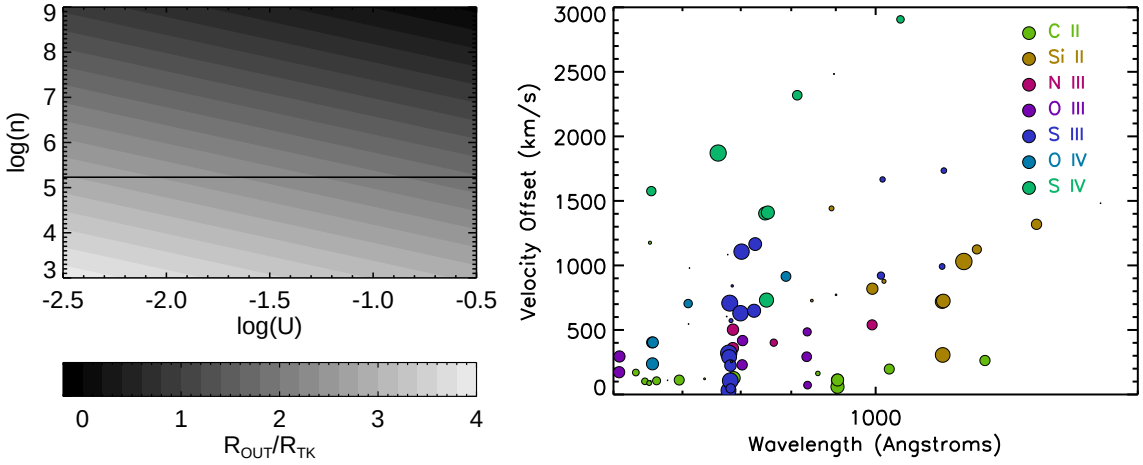

Fig. 15.— *Left:* The ratio of the outflow radius R_{out} to the K-band reverberation radius R_{TK} as a function of ionization parameter and hydrogen density. The solid line denotes the electron density $n_e = 1.7\times10^5\,\mathrm{cm}^{-3}$, which, as discussed in the text, is plausibly the largest density that can be securely measured using density-sensitive lines. Thus, only smaller densities and correspondingly larger radii can be explored using density-sensitive lines. *Right:* The velocity separation of adjacent lines with differing lower levels from a single ion as a function of wavelength of the shorter-wavelength line of each line pair. The symbol size is proportional to the log of the oscillator strength for the shorter-wavelength line of any line pair. This plot shows that velocity separations can be very small, due to the close spacing of the energy levels, and that the short wavelength region of the spectrum can be very crowded, and therefore, blending can be significant.

Blending can also significantly limit the use of density-sensitive lines. The broad absorption lines in FBQS J1151+3822 are significantly blended, and analysis of those lines requires assumptions that inevitably degrade the precision of the results. Since narrower lines will be less blended, objects studied using density-sensitive lines are often chosen on the basis of line width. Density-sensitive line pairs are often closely spaced, since the differences in the energies of the ground and excited state are small. Fig. 15 shows

the velocity separation of density-sensitive lines between 500 and 2000Å as a function of wavelength. Some lines, such as S III, have many transitions, and so the lines are closely packed, making measurements of individual lines difficult. Lines from different ions can be blended as well. Note that we did not include resonance lines with ground states originating in S terms, including, e.g., C IIIλ977, N IVλ765, the O Vλ630, Si IIIλ567, 1205, and S VIλ933, 945; these lines would increase the degree of blending further.

Perhaps there are no objects with narrow lines showing large ratios of excited state to ground state column densities (e.g., objects on the high-density asymptote in Fig. 15). But it may be that outflows characterized by broader lines, which would not be attractive candidates for density analysis, do have higher densities and originate closer to the central engine. This may make sense dynamically; if a BAL outflow is a transient event (Leighly et al. 2009; Filiz Ak et al. 2012), could it start near the nucleus with a high density, fragmenting, dispersing, and evaporating as the distance increases? It may be possible to test this idea by examining the S IV properties in, for example, BOSS quasars. The S IV pair of lines, at 1062 and 1073Å, has one of the widest separations available ($\sim 2900\,\mathrm{km\,s^{-1}}$). There are few lines close to and longward of this line pair, so the presence of the excited state can be clearly identified. Leighly et al. (2009) show that in WPVS 007, this line pair could be modeled using a template developed from the column-density sensitive lines P V$\lambda\lambda$1118, 1128. This could make sense because, although S IV is a slightly lower ionization line compared with P V and sulfur is about 100 times more abundant than phosphorus, the oscillator strengths of the S IV lines are about an order of magnitude lower than those of the P V lines. So these two ions might more likely be formed in a similar region of the outflow, and therefore might be expected to share similar kinematics and covering fraction. Finally, examining Fig. 6 in Leighly et al. (2009) shows that S IV* is strong in both WPVS 007 and comparison object LBQS 1212+1445, indicating high-density gas in both.

Thus, we conclude that FBQS J1151+3822, with its strong, blended excited-state absorption and correspondingly high density and small absorption radius, may not be genuinely unusual. Rather, the application of a density analysis to this object may be what is unusual. We chose to analyze FBQS J1151+3822 because we were interested in finding out what the newly discovered Fe II and Mg II absorption lines could tell us about the He I* absorption that we had previously reported, so it was not subject to this selection bias.

6. Summary

We obtained a KPNO spectrum of the He I* BALQSO FBQS J1151+3822 sampling short wavelengths approaching the atmospheric cutoff. We summarize our results below.

- The KPNO spectrum revealed broad, deep absorption centered near 2580 and 2750 Å. The shorter wavelength feature is mostly ground term Fe II. The longer wavelength feature contains Mg II and excited Fe II. These results demand reclassification of FBQS J1151+3822 as an FeLoBAL; it is, to our knowledge, the second-brightest ($m_V = 15.60$), second-closest ($z = 0.334$) known FeLoBAL after Mrk 231.

- We measured apparent ionic columns (Table 2, §3) of Mg II, Mg I, and two groups of Fe II excited levels (0–0.12 eV and 0.98–1.1 eV, which occur in largely disjoint parts of the spectrum), using He I* lines as templates for de-blending. The absorption model fit the spectrum well overall, although not in detail.

- We used the measured ionic columns and the photoionization code *Cloudy* to determine the physical properties of the absorbing gas. The extremely useful combination of He I*, produced in the H II region, and Fe II, produced beyond the hydrogen ionization front, pinpointed the ionization parameter at $\log U = -1.5$ (§4.1). The *Cloudy* parameter space demonstrated that Mg II is saturated. We found that

the He I*, Fe II, Fe II, and Mg I apparent columns were best matched at $\log U = -1.5$, $\log n = 7.2$, and $\log N_H - \log U = 23.18$, corresponding to $\log N_H = 21.68$ (§4.2). However, the consequently predicted ion columns did not yield an acceptable fit to the Fe II absorption spectrum, and we determined that Fe II is also saturated (§4.3), so that the best *Cloudy* fit provides only a lower limit on the hydrogen column density.

- To determine an upper limit on the hydrogen column density, we found an upper limit on absorption by low-opacity excited-state (0.98–1.72 eV) Fe II lines and excited-state (1.17 eV) Mn II near 2960Å (§4.4). The resultant upper limit on $\log(N_H) - \log(U)$ is 23.4, corresponding to an upper limit on $\log(N_H)$ of 21.9. The presence of broad, strong excited state Fe II implies a conservative lower limit on the density of $\log n \sim 5.5$ (§4.6).

- Using these results, we obtained lower and upper limits on the kinematic parameters of the BAL-producing outflow (§4.7). In contrast to Leighly et al. (2011), we were able to obtain constraints without making the unjustified assumption that the outflow is accelerated by radiative line driving. We found that the outflow radius is 7.2 to 127 parsecs, the mass flux 10.7 to 315 $\mathrm{M_\odot\,yr^{-1}}$, and the kinetic luminosity is 1×10^{44} to $28.9 \times 10^{44}\,\mathrm{erg\,s^{-1}}$ (0.16 to 4.5% of the bolometric luminosity).

- We estimated covering fractions to be around 0.6 for Mg II, 0.5 for He I*, and 0.25 for high-opacity Fe II (§4.4) with the differences yielding some preliminary insight into the geometric distribution of hydrogen column (§5.1). With more ions, similar future analyses might yield a constraint on the inhomogeneity of the gas.

- Narrow, rather shallow features appeared between the 2005 SDSS spectrum and the 2011 KPNO spectrum of this object in the $\sim$ 2900 to $\sim$ 2960Å range, which we identified as transitions of Mn II and high-excitation Fe II with velocities of $\sim 3,300\,\mathrm{km\,s^{-1}}$ (§3.4). These may signify condensation of higher-density clumps in

the outflow (§4.5). Additional mass, and therefore energy, may be hidden in these cores.

- Our analysis clarified the physical differences between HiBALs, LoBALs, and FeLoBALs (§4.3). For a given ionization parameter, HiBAL outflows have the smallest column, LoBAL outflows have a larger column (but Mg II LoBALs can still be truncated before the hydrogen ionization front is breached), and FeLoBAL outflows have the largest column (thicker, at least marginally, than the H II zone).

- In comparing our object to other well-studied FeLoBALs (§5.2), we found that the presence of Fe II 0.98–1.1 eV absorption indicates absorbing gas with density higher than critical and a distance from the nucleus on the order of tens-of-parsecs, while the absence of said absorption indicates absorbing gas with density lower than critical and a distance from the nucleus on the order of kiloparsecs. This absorption complex saturates over a small differential of physical parameter space, so a bimodality in this regard of FeLoBAL spectra does not necessarily indicate the bimodality of FeLoBAL physical properties posited in the literature. Thus, our object might not belong to a distinct low-radius subclass.

- The FBQS J1151+3822 outflow has higher density, and consequently smaller distance from the central engine, than most other intensively studied quasars—but this may be due to a selection bias in the literature. We investigated the use of density-sensitive lines, which have been used to conclude most outflows are located on kiloparsec scales. These lines have relatively low critical densities, and provide secure density estimates no higher than several times the critical density. Selecting for these lines, especially when unblended lines are preferred, may lead to a preference for large radii (§5.3).

We thank Pat Hall, Dick Henry, Eddie Baron, and Martin Elvis for useful discussions, and acknowledge Sara Barber's participation in the KPNO observing run. A.B.L. acknowledges funding by the Barry Goldwater Scholarship Foundation, and with K.M.L. acknowledges funding by the National Science Foundation. We thank the referee for helping us improve the clarity of this paper. This research has made use of the NASA/IPAC Infrared Science Archive, which is operated by the JPL, Caltech, under contract with NASA. This publication makes use of data products from the Wide-field Infrared Survey Explorer, which is a joint project of UCLA and JPL / Caltech, funded by NASA.

Facility: Mayall (R-C CCD Spectrograph)

A. The Host Galaxy Contribution to the Near IR

The one-micron region of an AGN or quasar spectrum is complicated. The accretion disk (assumed to emit a power law spectrum), the host galaxy, and the molecular torus can all contribute to varying degrees in this region (Landt et al. 2011). The BAL outflow is located at a smaller radius than the host galaxy, and therefore host galaxy light is unabsorbed by the BAL wind. If host galaxy emission is present in the spectrum coincident with the He I*λ10830 absorption line, the covering fraction will be underestimated.

The emission of the inner edge of the molecular torus, marked by an increase in flux toward longer wavelengths, is thought to be due to hot dust at the sublimation radius. The K-band reverberation radius, given by $R_{TK} = 0.47(6\nu L_{\nu}(5500\text{Å})/10^{46}\,\text{erg}\,\text{s}^{-1})^{1/2}\,\text{pc}$ (Kishimoto et al. 2011), can be substituted for the sublimation radius, and it is comparable with BAL outflow radii, generally speaking, so that the torus emission may or may not be absorbed. If it is not absorbed, but remains in the spectrum, the covering fraction will again be underestimated.

We did not take the host galaxy emission into account when estimating the He I* column in Leighly et al. (2011). Here, we rectify that oversight. We estimate the host galaxy and torus contributions, and then work through the remainder of the analysis presented in Leighly et al. (2011). We show that, while the average opacity and average covering fraction change when these components are accounted for, the average column density remains the same.

We estimated the contribution of the accretion disk and the torus to the integrated light of FBQS J1151+3822 by modeling available broadband photometry. This consisted of aperture magnitudes from the Sloan Digital Sky Survey, 2MASS, and WISE. FBQS J1151+3822 does not appear in the Spitzer and UKIDSS catalogs.

We first correct the SDSS and 2MASS photometry for emission and absorption lines. We proceed by first merging the SDSS, KPNO and IRTF spectra after having corrected for Galactic absorption. The merged spectrum was analyzed in segments corresponding to each filter. A minimum and maximum plausible continua was identified in each segment. The estimated continuum and the spectrum are then folded with the filter transmission curve, and the ratio of these gives a correction factor. The photometry was corrected using the mean of the minimum and maximum correction factors. One half the distance between the minimum and maximum correction factors was assigned as the uncertainty on the process of correcting for emission and absorption lines, and this was combined in quadrature with the photometry errors. We did not apply any correction to the WISE photometry, and note that those long wavelengths are less critical for determining the host galaxy contribution.

The individual magnitudes were converted to F_λ units using the calibrations in Fukugita et al. (1996) [SDSS], Cohen et al. (2003) [2MASS], and Jarrett et al. (2011) [WISE], then corrected for Galactic extinction using $E(B-V) = 0.024 \pm 0.004$ from Schlegel et al. (1998) and the optical/infrared reddening curve returned by IRAC, which

is based on A_λ/A_V information in Cardelli et al. (1988), O'Donnell (1994), and Lutz et al. (1996).

The line-corrected photometry was next corrected for Galactic reddening and then shifted to the rest frame. The resulting photometry of the continuum is shown in Fig. 16, along with the original values. The results were fit using Sherpa (Freeman et al. 2001) version 4.4 with a continuum model consisting of a power law for the accretion disk with $F_\lambda \propto \lambda^n$, a galaxy component consisting of a 13 Gyr single-burst population from PEGASE models (Fioc & Rocca-Volmerange 1997), a blackbody torus with temperature T_t, and a blackbody cool dust component with temperature T_d; the latter only contributes to the reddest two wavelengths from the WISE photometry. We ran a series of models in which the internal reddening for the AGN was fixed at various values $E(B-V)$, as follows. Quasar reddening curves are often inferred to be steep, more like the SMC than like Milky Way dust (e.g., Crenshaw et al. 2001). We implemented an SMC-like reddening function from Prevot et al. (1984). The spectral fitting model was degenerate in the power law slope, reddening, and galaxy template normalization. Therefore, we fixed the reddening to two values: $E(B-V) = 0.14$, derived based on the shape of the blue part of the optical spectrum, as derived above, and $E(B-V) = 0.26$, based on the ratio of the Balmer lines (observed to be 4.00) assuming an intrinsic ratio of 3.06 and an SMC reddening curve. While the Balmer decrement may seem to better estimate the intrinsic reddening, note that it is not clear that the broad line region is subject to the same reddening as the continuum, or that the intrinsic ratio of the Balmer lines is 3.06 (e.g., Popović 2003). Nevertheless, these two values provide useful bounds.

Table 5 displays the results of the fits to the SED using these two values of $E(B-V)$, and for an intermediate value of $E(B-V) = 0.20$, and the derived fraction of the contribution of the dusty torus and accretion disk to the continuum flux at $\lambda_0 = 10830$Å.

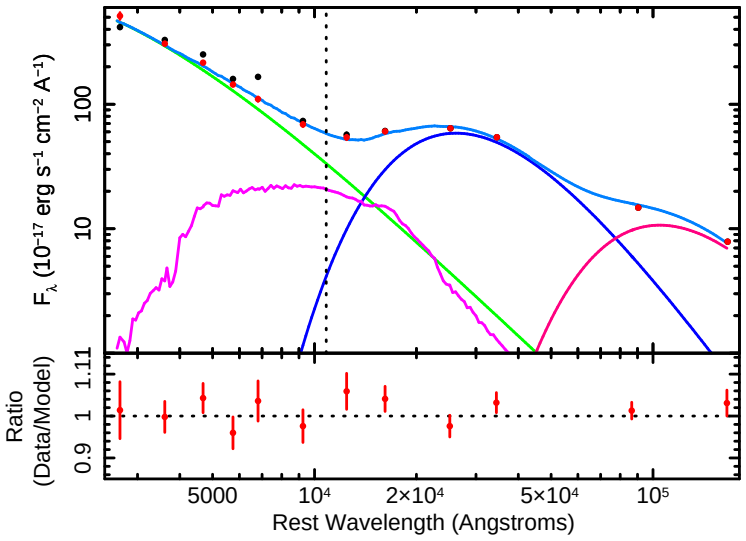

Fig. 16.— The SDSS, 2MASS and WISE photometry fit with a model consisting of a power law (green line), two blackbodies (blue and red lines), and an elliptical template (fuchsia), all reddened by SMC-type extinction with $E(B-V) = 0.2$ (see §A). The black points give the raw photometry (corrected for Milky Way extinction and redshift), and the red points give the photometry corrected for emission or absorption lines in the bandpass. At rest frame 10830Å (marked by the vertical line) the torus hot dust (i.e., warmer black body) and the host galaxy each contribute 7.1% and 35.6% of the continuum, respectively. This result is largely insensitive of the value of E(B-V) (see Table 5).

The derived slope of the accretion disk SED and the starlight contribution of the disk to the continuum at the infrared helium line are, as expected, dependent on the assumed internal reddening; higher values of $E_0(B-V)$ require steeper power laws for the accretion disk and result in a larger fraction of host galaxy. The derived temperature of the AGN torus and the fraction of light contributed by the torus are, however, largely insensitive to the assumed extinction values. If the reddening is within the assumed range, then the contribution of the accretion disk and torus to the continuum at $\lambda_{rest} = 10830$Å is 0.42 ± 0.04. Consideration of alternative extinction SMC extinction laws such as Pei (1992) and Gordon et al. (2003) produced somewhat different values of the starlight/torus contribution, which we characterize as an additional systematic error, resulting in a final

estimated contribution of 0.42 ± 0.04 (fitting) ± 0.06 (systematic). A plot of the fit for the intermediate value of the extinction is shown in Fig. 16.

We consider two cases: the torus is absorbed by the outflow, and the galaxy is not, and both the torus and galaxy are not absorbed. We first create the ratio of the galaxy (with and without the torus) to the total model, and transform that to velocity space for a rest wavelength of 10830.171Å. We resample that on the velocities derived from the original IRTF spectrum (shown in Fig. 3 in Leighly et al. 2011). We then subtract this ratio from the profile and renormalize by dividing by one minus the ratio. The uncertainties assigned to the new I/I_0 ratios were taken to be half the difference in the values obtained by propagating the original I/I_0 values plus and minus the original uncertainties. As in Leighly et al. (2011), we considered four profiles for the 3889Å line (obtained from two Fe II models applied to the SDSS spectrum and a later MDM spectrum); see Leighly et al. (2011) for details.

The obtained average covering fraction ranged from 0.26 to 0.28 without continuum

Table 5. SED fitting results

	$E_0(B-V)$		
Quantity	0.14	0.20	0.26
Accretion disk slope	-2.33 ± 0.015	-2.59 ± 0.013	-2.84 ± 0.012
Torus temperature (K)	1127 ± 29	1129 ± 29	1132 ± 30
Torus fraction	0.073 ± 0.003	0.072 ± 0.003	0.070 ± 0.002
Starlight fraction	0.31 ± 0.08	0.35 ± 0.08	0.39 ± 0.09
χ^2_n	2.03	1.88	1.75

subtractions (Leighly et al. 2011), from 0.43 to 0.50 with the galaxy subtracted from the continuum, and from 0.48 to 0.51 with the galaxy and torus subtracted. The *average* column density, which for the step-function partial covering model is equal to the covering fraction times the column density of the covered fraction, is much the same no matter whether we subtract the galaxy, the torus plus the galaxy, or nothing; the fit responds to the subtraction of continuum components by producing a lower average column density and higher average covering fraction. Therefore, we continue to use 14.9 as the value the log of the He I* column density, as we did in Leighly et al. (2011).

REFERENCES

Arav, N., Borguet, B., Chamberlain, C., Edmonds, D., & Danforth, C. 2013, MNRAS, 436, 3286

Arav, N., Kaastra, J., Kriss, G. A., et al. 2005, ApJ, 620, 665

Arav, N., Korista, K. T., de Kool, M., Junkkarinen, V. T., & Begelman, M. C. 1999, ApJ, 516, 27

Arav, N., Moe, M., Costantini, E., et al. 2008, ApJ, 681, 954

Becker, R. H., Gregg, M. D., Hook, I. M., et al. 1997, ApJ, 479, L93

Becker, R. H., White, R. L., Gregg, M. D., et al. 2000, ApJ, 538, 72

Borguet, B. C. J., Arav, N., Edmonds, D., Chamberlain, C., & Benn, C. 2013, ApJ, 762, 49

Borguet, B. C. J., Edmonds, D., Arav, N., Benn, C., & Chamberlain, C. 2012, ApJ, 758, 69

Canalizo, G., & Stockton, A. 2001, ApJ, 555, 719

Capellupo, D. M., Hamann, F., Shields, J. C., Rodríguez Hidalgo, P., & Barlow, T. A. 2011, MNRAS, 413, 908

Cardelli, J. A., Clayton, G. C., & Mathis, J. S. 1988, ApJ, 329, L33

—. 1989, ApJ, 345, 245

Casebeer, D. A., Leighly, K. M., & Baron, E. 2006, ApJ, 637, 157

Cavaliere, A., Lapi, A., & Menci, N. 2002, ApJ, 581, L1

Cohen, M., Wheaton, W. A., & Megeath, S. T. 2003, AJ, 126, 1090

Crenshaw, D. M., Kraemer, S. B., Bruhweiler, F. C., & Ruiz, J. R. 2001, ApJ, 555, 633

de Kool, M., Arav, N., Becker, R. H., et al. 2001, ApJ, 548, 609

de Kool, M., Becker, R. H., Arav, N., Gregg, M. D., & White, R. L. 2002a, ApJ, 570, 514

de Kool, M., Becker, R. H., Gregg, M. D., White, R. L., & Arav, N. 2002b, ApJ, 567, 58

Dunn, J. P., Bautista, M., Arav, N., et al. 2010, ApJ, 709, 611

Emmering, R. T., Blandford, R. D., & Shlosman, I. 1992, ApJ, 385, 460

Farrah, D., Lacy, M., Priddey, R., Borys, C., & Afonso, J. 2007, ApJ, 662, L59

Farrah, D., Urrutia, T., Lacy, M., et al. 2012, ApJ, 745, 178

Ferland, G. J., Korista, K. T., Verner, D. A., et al. 1998, PASP, 110, 761

Ferland, G. J., Porter, R. L., van Hoof, P. A. M., et al. 2013, Rev. Mexicana Astron. Astrofis., 49, 137

Filiz Ak, N., Brandt, W. N., Hall, P. B., et al. 2012, ApJ, 757, 114

Fioc, M., & Rocca-Volmerange, B. 1997, A&A, 326, 950

Francis, P. J., Hewett, P. C., Foltz, C. B., et al. 1991, ApJ, 373, 465

Frank, J., King, A., & Raine, D. J. 2002, Accretion Power in Astrophysics: Third Edition

Freeman, P., Doe, S., & Siemiginowska, A. 2001, in Society of Photo-Optical Instrumentation Engineers (SPIE) Conference Series, Vol. 4477, Society of Photo-Optical Instrumentation Engineers (SPIE) Conference Series, ed. J.-L. Starck & F. D. Murtagh, 76–87

Fukugita, M., Ichikawa, T., Gunn, J. E., et al. 1996, AJ, 111, 1748

Gabel, J. R., Kraemer, S. B., Crenshaw, D. M., et al. 2005, ApJ, 631, 741

Gallagher, S. C., Brandt, W. N., Chartas, G., et al. 2006, ApJ, 644, 709

Gibson, R. R., Jiang, L., Brandt, W. N., et al. 2009, ApJ, 692, 758

Gordon, K. D., Clayton, G. C., Misselt, K. A., Landolt, A. U., & Wolff, M. J. 2003, ApJ, 594, 279

Green, P. J., Aldcroft, T. L., Mathur, S., Wilkes, B. J., & Elvis, M. 2001, ApJ, 558, 109

Gregg, M. D., Becker, R. H., & de Vries, W. 2006, ApJ, 641, 210

Hamann, F., Barlow, T. A., Junkkarinen, V., & Burbidge, E. M. 1997, ApJ, 478, 80

Hamann, F., Chartas, G., McGraw, S., et al. 2013, MNRAS, 435, 133

Hamann, F., Korista, K. T., Ferland, G. J., Warner, C., & Baldwin, J. 2002, ApJ, 564, 592

Hamann, F. W., Barlow, T. A., Chaffee, F. C., Foltz, C. B., & Weymann, R. J. 2001, ApJ, 550, 142

Hazard, C., McMahon, R. G., Webb, J. K., & Morton, D. C. 1987, ApJ, 323, 263

Jarrett, T. H., Cohen, M., Masci, F., et al. 2011, ApJ, 735, 112

Jester, S., Schneider, D. P., Richards, G. T., et al. 2005, AJ, 130, 873

Kishimoto, M., Hönig, S. F., Antonucci, R., et al. 2011, A&A, 536, A78

Konigl, A., & Kartje, J. F. 1994, ApJ, 434, 446

Korista, K., Baldwin, J., Ferland, G., & Verner, D. 1997, ApJS, 108, 401

Korista, K. T., Bautista, M. A., Arav, N., et al. 2008, ApJ, 688, 108

Korista, K. T., Weymann, R. J., Morris, S. L., et al. 1992, ApJ, 401, 529

Kriss, G. 1994, Astronomical Data Analysis Software and Systems, 3, 437

Landt, H., Elvis, M., Ward, M. J., et al. 2011, MNRAS, 414, 218

Leighly, K. M. 2004, ApJ, 611, 125

Leighly, K. M., Dietrich, M., & Barber, S. 2011, ApJ, 728, 94

Leighly, K. M., Halpern, J. P., Jenkins, E. B., & Casebeer, D. 2007, ApJS, 173, 1

Leighly, K. M., Hamann, F., Casebeer, D. A., & Grupe, D. 2009, ApJ, 701, 176

Leighly, K. M., Lucy, A. B., Dietrich, M., Terndrup, D., & Gallagher, S. C. 2012, ArXiv e-prints, arXiv:1203.6663

Leighly, K. M., & Moore, J. R. 2006, ApJ, 644, 748

Lutz, D., Feuchtgruber, H., Genzel, R., et al. 1996, A&A, 315, L269

Moe, M., Arav, N., Bautista, M. A., & Korista, K. T. 2009, ApJ, 706, 525

Moore, C. E. 1952, An ultraviolet multiplet table

Morabito, L. K., Dai, X., Leighly, K. M., Sivakoff, G. R., & Shankar, F. 2011, ApJ, 737, 46

O'Donnell, J. E. 1994, ApJ, 422, 158

Pei, Y. C. 1992, ApJ, 395, 130

Popović, L. Č. 2003, ApJ, 599, 140

Prevot, M. L., Lequeux, J., Prevot, L., Maurice, E., & Rocca-Volmerange, B. 1984, A&A, 132, 389

Richards, G. T., Lacy, M., Storrie-Lombardi, L. J., et al. 2006, ApJS, 166, 470

Sabra, B. M., & Hamann, F. 2005, ArXiv Astrophysics e-prints, arXiv:astro-ph/0509421

Savage, B. D., & Sembach, K. R. 1991, ApJ, 379, 245

Scannapieco, E., & Oh, S. P. 2004, ApJ, 608, 62

Schlegel, D. J., Finkbeiner, D. P., & Davis, M. 1998, ApJ, 500, 525

Trump, J. R., Hall, P. B., Reichard, T. A., et al. 2006, ApJS, 165, 1

Voit, G. M., Weymann, R. J., & Korista, K. T. 1993, ApJ, 413, 95

Wampler, E. J., Chugai, N. N., & Petitjean, P. 1995, ApJ, 443, 586

Weymann, R. J., Morris, S. L., Foltz, C. B., & Hewett, P. C. 1991, ApJ, 373, 23

This manuscript was prepared with the AAS LaTeX macros v5.2.